A non-hydrostatic non-Boussinesq algorithm for free-surface ocean modelling

Francis Auclair, Lucie Bordois, Yvan Dossmann, Thomas Duhaut, Alexandre Paci, Caroline Ulses, Cong Tu Nguyen

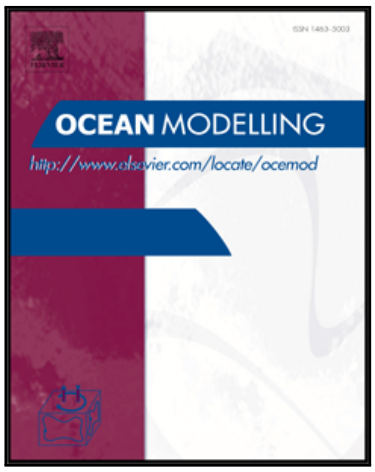

A non-hydrostatic non-Boussinesq algorithm for free-surface ocean modelling

F. Auclair , L. Bordois , Y. Dossmann , T. Duhaut , A. Paci , C. Ulses , C. Nguyen

PII: S1463-5003(18)30264-6
DOI: https://doi.org/10.1016/j.ocemod.2018.07.011
Reference: OCEMOD 1327

To appear in: *Ocean Modelling*

Received date: 6 July 2017
Revised date: 25 July 2018
Accepted date: 31 July 2018

Please cite this article as: F. Auclair , L. Bordois , Y. Dossmann , T. Duhaut , A. Paci , C. Ulses , C. Nguyen , A non-hydrostatic non-Boussinesq algorithm for free-surface ocean modelling, *Ocean Modelling* (2018), doi: https://doi.org/10.1016/j.ocemod.2018.07.011

Highlights

- An original time-split approach is implemented in a free-surface ocean model.
- NH flows are simulated in a natural way, propagating acoustic waves.
- The three-mode algorithm is detailed and its performances are evaluated.
- Acoustic, surface-gravity and internal-gravity waves are studied

A non-hydrostatic non-Boussinesq algorithm for free-surface ocean modelling

Auclair F.[1], L. Bordois[1,2], Y. Dossmann[2,1], T. Duhaut[1], A. Paci[2] , C. Ulses[1] and C. Nguyen[1]

[1] Laboratoire d'Aérologie, Université de Toulouse, CNRS, UPS, France. Corresponding author: Francis Auclair : francis.auclair@aero.obs-mip.fr, Tel.: (33) 561332775, Fax: (33) 561332790.

[2] CNRM-GAME, GMEI, SPEA, CNRS, Météo-France, Toulouse, France

Abstract

A three-mode time-split algorithm is proposed to simulate non-hydrostatic ocean processes in a natural way: fast pressure adjustments via acoustic waves are explicitly represented. The full set of compressible Navier-Stokes equations is integrated for a free-surface ocean with three time-steps respectively associated to the internal, external and compressible (non Boussinesq) modes. The resulting three-mode algorithm can be implemented either in a fully compressible configuration or in a "pseudo-compressible" configuration by artificially lowering acoustic-wave velocities to reduce computational costs. The present description of the three-mode algorithm focuses in the first place on the simulation of non-hydrostatic processes in free-surface ocean models.

Several test simulations related to linear and non-linear acoustic, surface and internal gravity waves are studied in details with the proposed three-mode algorithm.

1 Introduction

Fast pressure adjustments in fluids occur primarily through acoustic waves. These adjustments are closely related to the bulk compressibility of fluid and the system of Navier-Stokes equations includes physical processes at all ocean scales spreading from general circulation to high-velocity sound waves not to mention surface gravity waves.

In the last decades, three types of approaches have basically been proposed to deal with acoustic waves in weather forecast models. To filter these high-velocity waves, Ogura and Phillips (1962) and many others ever since, imposed the anelastic approximation. As a consequence, a global 3D Poisson system has to be solved at every time-step. Durran and Blossey (2012) did not impose such approximation and proposed to simulate high-velocity acoustic waves using an Implicit-Explicit multistep method: Courant number restrictions are circumvented using an implicit scheme but a global Helmholtz 3D equation must be solved. Avoiding solving large 3D systems of equations, Janjic (2003) proposed this time to simulate explicitly acoustic waves based on a time-split approach. Propagation of sound waves is permitted with a small, Courant-number limited, time-step and a large time-step is used for atmospheric slower processes. All those approaches have in common the necessity to simulate the consequences of the transient adjustments due to acoustic waves but they all care much less about the details of the propagation of the acoustic waves: only the result of the faster transients is then of interest. Still with the objective to limit Courant number restrictions, Chorin (1967) proposed to reduce acoustic wave velocity, leading to an artificial compressibility. Several atmospheric numerical models (see Skamarock and Klemp, 2008 for a complete list) can thus simulate faster pressure adjustments in a natural way. These models are particularly well-adapted to modern, massively parallel computing: they are based on local (in space and time) equations and do not require solving global systems.

In non-hydrostatic ocean models, pressure-correction, Boussinesq algorithms have been preferred since Marshall et al. (1997). Because acoustic waves are four to five times slower in the atmosphere than in the ocean, one could at first conclude that their simulation imposes stronger Courant-number restrictions in the ocean and that it is consequently much more expensive than in the atmosphere. The treatment of bulk compressibility and acoustic waves are of the same nature in the atmosphere and in the ocean but the spectral gap between faster incompressible dynamics and acoustic waves is larger in the ocean.

"Non-hydrostatic effects" are naturally associated to acoustic waves. As a consequence, acoustic wave dynamics can be viewed as a natural solver for hydrodynamic pressure. In the same way as in atmospheric models, the consequences of the transient compressible adjustments of pressure are of interest and we propose to retain bulk compressibility (or at least artificial or pseudo-compressibility) to simulate non-hydrostatic pressure adjustments in otherwise incompressible ocean configurations. The main originality compared to atmospheric models lies in the implementation of a compressible ("non Boussinesq") mode in a free-surface

ocean model which is already based on a barotropic / baroclinic time-split approach. This leads to a "three-mode time-split algorithm".

A three-mode time-split algorithm

Since Blumberg and Mellor (1987), most ocean models simulate long surface gravity waves with a barotropic / baroclinic time-splitting. We propose to make one further step in this time-split strategy by implementing a third, compressible (non-Boussinesq) mode in the barotropic (hereafter external) mode, this 2D mode remaining itself embedded in the slow, baroclinic (hereafter internal) mode. The resulting "three-mode algorithm" is consequently based on three time-steps, the smaller being dedicated the fast (3D) dynamics of acoustic (or pseudo-acoustic) waves. This leads to a limited number of modifications in existing numerical models: (i) the Boussinesq or Anelastic approximations must be abandoned, (ii) momentum rather than velocity becomes a prognostic variable, (iii) the vertical velocity must be prognosticated at the internal mode time-step through the corresponding momentum equation and (iv) the time-splitting must be extended to include a third, faster, compressible mode to propagate acoustic waves. In its present implementation, the three-mode algorithm is however less general than a full Navier-Stokes model as only the linear (advection-free) acoustic part of the dynamics is solved with a small time-step and the sound speed remains constant, requiring temperature and salinity to be computed only at the larger internal-mode time-step.

Hydrostatic assumption

We can wonder why, in the first place, the hydrostatic assumption should be revoked in ocean models. The reason is essentially to provide an accurate description of wave dynamics and to introduce non-hydrostatic processes such as vertical motions in convective chimneys (Marshall and Schott, 1999), non-hydrostatic dispersion in solitary waves (Lamb, 2004) or the "non-traditional" component of the Coriolis force leading to more accurate representation of the vorticity balance (Gerkema et al., 2007). Following Vallis (2006, Chapter 2.7), it can be shown that, to be in hydrostatic equilibrium, a homogeneous ocean must have small aspect ratio $(\varepsilon \equiv H/L << 1)$ with H and L the vertical and horizontal length scales whereas a stratified ocean must satisfy $(Fr^2\varepsilon^2 << 1)$ with $Fr \equiv V/NH$, N a typical Brunt-Väisälä frequency and V an horizontal velocity scale. Several approaches have been proposed to circumvent the hydrostatic approximation for a Boussinesq flow (Marshall et al., 1997; Casulli 1999; Auclair et al. 2011). Pure pressure-projection (Boussinesq) algorithms (Chorin, 1967) require to first step-forward momentum equations before adjusting the non-hydrostatic pressure. A 3D Poisson system must then be solved for. Pressure-correction methods additionally require that an up-to-date non-hydrostatic pressure force is taken into account when advancing momentum equations (first step) and only an increment of the non-hydrostatic pressure is calculated by solving for the 3D Poisson system (Dukowicz and Dvinsky, 1992; Mahadevan et al. (1996); Marshall et al. (1997) and many others…). An additional difficulty with non-hydrostatic modelling in free-surface ocean models is associated to the strong coupling of the non-hydrostatic and surface-induced components of the pressure field (Auclair et al.,

2011). To our knowledge, none of these non-hydrostatic algorithms is based on an explicit simulation of acoustic waves in the context of a free-surface ocean.

Boussinesq assumption

Large to regional scale ocean models most often rely on both the Boussinesq and hydrostatic assumptions leading to a description of the ocean in which buoyancy has a central role. In more or less the same way as the anelastic approximation restricts the range of atmospheric processes, the Boussinesq assumption is justified by the small deviations of the ocean density from a reference value and it provides an efficient framework to study slow, large-scale processes which are characterized by small vertical-to-horizontal length-scale ratios. It basically decouples the dynamics and thermodynamics of the ocean, filters out acoustic waves and leads to a mathematical degeneracy of the non-hydrostatic system of equations: the filtering of the acoustic waves transforms the initially hyperbolic system of equations into an elliptical system. Boussinesq flows conserve volume but not mass, leading to discrepancies in the transient adjustment processes following for instance the surface heating of the ocean (Huang and Jin, 2002). Another consequence of the Boussinesq assumption concerns the way energy is transferred between the kinetic and potential compartments (Tailleux, 2010).

When combined, the Boussinesq and hydrostatic assumptions provide a simple, valuable and accurate representation of "slow and large scale" ocean processes. Nevertheless, the access to ever more efficient computing facilities associated to the desire to improve the simulated dynamics by –for instance- extending the space-time spectrum toward "high-frequencies and small-scales" lead oceanographers to question and then circumvent these assumptions (Shchepetkin and McWilliams, 2011, Section 5). Greatbatch et al. (2001) propose to reconsider the concept of velocity: to conserve mass, velocity should indeed not be considered as the result of a Reynolds averaging but rather as the result of a Favre averaging. When the objective is mainly to recover the non-Boussinesq steric effect under the hydrostatic assumption without reintroducing the acoustic waves, DeSzoeke and Samelson (2002) have shown that pressure coordinates constitute a valuable choice. A divergent formulation of the velocity field can instead be obtained by improving the accuracy with respect to the density anomalies (Dewar et al., 2015). These aspects are not further investigated "numerically" hereafter: the modelling of the steric effect with the present three-mode non-Boussinesq algorithm should be investigated in a following study.

Following time-split approaches currently implemented in weather forecast models and adapting these approaches to the context of a free-surface ocean, we propose to abandon both the hydrostatic and Boussinesq approximations. First of all, the acoustic waves are reintroduced in order to recover mathematical hyperbolicity. From this standpoint, the proposed algorithm can thus be viewed as a "physical solver" for non-hydrostatic ocean flows. In terms of parallel computing, a consequence is that computations are local in space. Limiting the perspectives to a simple reduction of computational cost would be over-simplistic since conservation of mass can also be advantageously recovered by integrating in time the full continuity equation. The proposed algorithm additionally leads to the recovering of a physical (i.e. non-Boussinesq) treatment of

the kinetic to internal and gravitational potential energy exchanges. The three-mode algorithm provides de facto another way to deal with the pressure dependence of the EOS by re-introducing a first-order pressure dependence of the density.

Second viscosity is also reintroduced in the momentum equations since velocity divergence does not vanish any more: the corresponding damping process can be considered as an efficient (natural) filter for acoustic waves. This second-viscosity filter is equivalent to the selective numerical filter proposed by Skamarock and Klemp (1992) to damp "divergent modes" in their atmospheric model.

Section 2 is dedicated to the density and pressure decomposition, the Non-Boussinesq mode-splitting algorithm is then described in details in Section 3. Auclair et al. (2011)'s test configurations and the compressible configurations of acoustic waves are revisited in Section 4. Discussion and conclusions are finally given in Section 5.

2 From compressible Navier-Stokes Equations to Boussinesq Assumption

2.1 Compressible Navier-Stokes equations

Full compressible Navier-Stokes system in Cartesian (z-) coordinates is given by:

$$\rho\frac{d\vec{v}}{dt} = -\vec{\nabla}p + \rho\vec{g} + \delta\vec{F}_c + \rho\nu\Delta\vec{v} + \rho\lambda\vec{\nabla}\left(\vec{\nabla}.\vec{v}\right) \qquad (1a)$$

$$\frac{\partial\rho}{\partial t} = -\vec{\nabla}.(\rho\vec{v}) \qquad (1b)$$

$$\frac{d(\theta,S)}{dt} = \left(\phi^{(\theta)},\phi^{(S)}\right) \qquad (1c)$$

$$\rho = \rho(\theta,S,p) \qquad (1d)$$

where $\vec{v}=(u,v,w)$ is the velocity, p the total pressure, ρ the density, θ the potential temperature, S the salinity, ν the (constant) kinematic viscosity and λ the (constant) bulk or "second" viscosity (hereafter both viscosities are assumed homogeneous to simplify notations). The second velocity participates to the damping of acoustic waves. The Lagrangian derivative of momentum varies according to Equation (1a) with the pressure force, the weight, the Coriolis pseudo-force and the viscous diffusion. The second-viscosity diffusion is an efficient filter in term of numerical cost whereas it is also the "natural filter" for acoustic waves. On the right-hand side (RHS) of the heat and salinity evolution equations (1c), $\phi^{(\theta)}$ and $\phi^{(S)}$ gather compressibility

and diabatic processes[3]. The last equation is the general EOS for seawater: density is a function of potential temperature, salinity and (total) pressure. The Coriolis pseudo-force can be written in a compact form ($\vec{\Omega}$ being the earth angular velocity):

$$\delta\vec{F}_c = -2\rho\vec{\Omega}\wedge\vec{v} \qquad (2)$$

At the surface of the ocean, the boundary condition is given by the continuity of the pressure field and viscous stress tensor. The presence of a free-surface additionally imposes a non-trivial kinematic condition at $z=\zeta$ with ζ the free-surface anomaly:

$$w(z=\zeta)=\frac{\partial\zeta}{\partial t}+u(z=\zeta)\frac{\partial\zeta}{\partial x}+v(z=\zeta)\frac{\partial\zeta}{\partial y} \qquad (3)$$

At the bottom $(z=-H)$ with H the ocean depth, the no-permeability kinematic condition leads to:

$$w(z=-H)=-u(z=-H)\frac{\partial H}{\partial x}-v(z=-H)\frac{\partial H}{\partial y} \qquad (4)$$

The depth-integral of the continuity equation (1b) can be combined with the kinematic conditions (3) and (4) to obtain an evolution equation for the mass of a water column:

$$\frac{\partial(H+\zeta)\overline{\rho}}{\partial t}=-\frac{\partial(H+\zeta)\overline{\rho u}}{\partial x}-\frac{\partial(H+\zeta)\overline{\rho v}}{\partial y} \qquad (5)$$

where the overbar stands for (vertical) depth-average over the water column.

2.2 Boussinesq approximation

The formulation of the Boussinesq assumption first requires that a thermodynamical equilibrium state be chosen as a reference. The corresponding reference density ρ_0 is homogeneous and stationary. The Boussinesq approximation then requires that:

- (BQ-i) density anomalies $(\rho-\rho_0)$ are negligible with respect to the reference density,
- (BQ-ii) the vertical scale (H_ρ) over which this density field varies is much larger than the ocean vertical scales: $H_\rho^{-1}\equiv\frac{1}{\rho}\frac{\partial\rho}{\partial z}<<H^{-1}$.

Both requirements are satisfied with a reasonable accuracy (less than a few percent) by large-scale fields whereas atmospheric dynamics is commonly studied using the less-restrictive anelastic assumption (BQ-i). Under the Boussinesq assumption, the compressible Navier-Stokes system (1)–(5) simplifies to:

[3] Following for instance Griffies (2004, chapter 5), right-hand side of (1c) can be decomposed in a diffusion flux and a source term.

$$\frac{d\vec{v}}{dt} = -\frac{1}{\rho_0}\vec{\nabla} p + \frac{\rho}{\rho_0}\vec{g} - 2\vec{\Omega} \wedge \vec{v} + \nu\Delta\vec{v} \qquad (6a)$$

$$\vec{\nabla}.\vec{v} = 0 \qquad (6b)$$

$$\frac{d(\theta, S)}{dt} = \left(\phi^{(\theta)}, \phi^{(S)}\right) \qquad (6c)$$

$$\rho = \rho_{bq}(\theta, S, -\rho_0 gz) \qquad (6d)$$

Thermodynamically speaking, the Boussinesq equation of state (6d) for seawater can only relate density, temperature and salinity to an approximation of pressure (the high-frequency component of the total pressure field being filtered out) leading to the so-called "seawater Boussinesq approximation" (Young, 2010). The Boussinesq assumption has several additional consequences recalled in Appendix A.

2.3 Density and pressure decomposition

First order pressure dependence can be retained in EOS (1d):

$$\rho = \rho(\theta, S, p) = \rho_0 + \rho_{bq}(\theta, S, p_{ref}) + \underbrace{\left.\frac{\partial \rho}{\partial p}\right|_{\theta,S} \delta p}_{\delta\rho} + O(\delta p^2) \qquad (7)$$

where $\left.\frac{\partial \rho}{\partial p}\right|_{\theta,S} = \frac{1}{c_s^2}$ with $c_s(\theta, S, p) = \sqrt{\left.\frac{\partial p}{\partial \rho}\right|_{\theta,S}}$ the velocity of acoustic waves and p_{ref} is a chosen reference pressure. A decomposition of the pressure field follows:

$$p = p_{atm} + \underbrace{\rho_0 g(\zeta - z) + \int_z^\zeta (\rho_{bq} - \rho_0) g dz'}_{p_h} + \delta p \qquad (8)$$

with p_{atm} the atmospheric pressure at the surface of the ocean, p_h the hydrostatic component based on the Boussinesq component of density and δp the non-hydrostatic increment of pressure. The reference pressure (p_{ref}) must then be chosen. For the numerical configurations presented in the following, the reference pressure is the hydrostatic pressure for a homogeneous, constant reference density; it is equal to the depth-dependent reference pressure used in the Boussinesq EOS (6d), i.e.:

$$p_{ref} = -\rho_0 gz \qquad (9)$$

For the same type of expansion, Dewar et al. (2015) choose the static pressure caused by P_{atm} and by a mean density profile as a reference pressure.

Because the sound speed $c_s(\theta, S, p)$ depends on the potential temperature, salinity and pressure, the "compressible" or "non-Boussinesq" pressure (δp) and density $(\delta\rho)$ anomalies are not linearly correlated in a general case. We disregard this dependence in the experiments that follow for simplicity.

Considering for simplicity that atmospheric pressure is also constant, the non-Boussinesq system of equations can now be written in a conservative form:

$$\frac{\partial \rho \vec{v}}{\partial t} = -\frac{\partial \rho u \vec{v}}{\partial x} - \frac{\partial \rho v \vec{v}}{\partial y} - \frac{\partial \rho w \vec{v}}{\partial z} - \vec{\nabla}^{(h)} p_h - \vec{\nabla}\delta p + \delta\rho \vec{g} + \delta\vec{F}_c + \rho\nu\Delta\vec{v} + \rho\lambda\vec{\nabla}\left(\vec{\nabla}.\vec{v}\right) \qquad (10a)$$

$$\frac{\partial \rho}{\partial t} = -\vec{\nabla}.\{\rho\vec{v}\} \qquad (10b)$$

$$\frac{\partial \rho(\theta, S)}{\partial t} = -\frac{\partial \rho u(\theta, S)}{\partial x} - \frac{\partial \rho v(\theta, S)}{\partial y} - \frac{\partial \rho w(\theta, S)}{\partial z} + \rho\left(\phi^{(\theta)}, \phi^{(S)}\right) \qquad (10c)$$

$$\rho = \rho(\theta, S, p) = \rho_{bq}(\theta, S, -\rho_0 gz) + \underbrace{\left.\frac{\partial \rho}{\partial p}\right|_{\theta,S} \delta p}_{\delta\rho} \qquad (10d)$$

where $\vec{\nabla}^{(h)}$ is the horizontal component of the gradient in Cartesian coordinates.

The decomposition of density (10d) is thus partially in line with the expansion proposed by Dewar et al. (2015) but p_h is here supposed to be in hydrostatic equilibrium with ρ_{bq} whereas Dewar et al. more generally consider that the Boussinesq field can be at least partly non-hydrostatic. The proposed algorithm also differs from theirs by retaining the full expression of the continuity equation and, as a consequence, the acoustic waves. No additional terms need to be implemented in the present vertical momentum equations to provide an accurate kinetic to internal energy conversion.

The decomposition of the pressure field can finally be compared with the one used in a pressure-correction algorithm:

$$p = \underbrace{p_{atm} + \rho_0 g(\zeta - z) + \int_z^\zeta (\rho_{bq} - \rho_0) g dz'}_{p_h} + q \qquad (11)$$

where q is the "Boussinesq" non-hydrostatic "pressure correction" obtained by solving a 3D Poisson system. In Equation 8, δp is the non-hydrostatic pressure increment linearly associated to the non-hydrostatic density anomaly $\delta\rho$ through (10d).

3 The three-mode non-hydrostatic algorithm

The three-mode splitting algorithm is now detailed and we implement it into a Boussinesq, hydrostatic, free-surface ocean models already based on a baroclinic / barotropic time-splitting. In the first place, this algorithm aims at simulating fast pressure adjustments leading to non-hydrostatic dynamics.

3.1 Decomposition of the momentum equations

Momentum equations (10a) include in their RHS both "slow", "fast" and "very fast" terms respectively computed in the internal, external and "compressible" or "Non-Boussinesq" (NBQ)-modes:

$$\frac{\partial \rho \vec{v}}{\partial t} = \vec{\Lambda}_i^{'} + \vec{\Lambda}_e + \vec{\Lambda}_q \qquad (12)$$

The operators $\vec{\Lambda} = \left(\Lambda_x, \Lambda_y, \Lambda_z\right)$ can be written (13a):

$$\vec{\Lambda}_i \equiv -\frac{\partial \rho u \vec{v}}{\partial x} - \frac{\partial \rho v \vec{v}}{\partial y} - \frac{\partial \rho w \vec{v}}{\partial z} - \vec{\nabla}^{(h)} p_h + \delta \vec{F}_c + \rho \nu \Delta \vec{v} \qquad (13a)$$

$$\vec{\Lambda}_q \equiv -\vec{\nabla}\delta p + \delta\rho \vec{g} + \rho\lambda\vec{\nabla}\left(\vec{\nabla}.\vec{v}\right) = -c_s^2 \vec{\nabla}\delta\rho + \delta\rho \vec{g} + \rho\lambda\vec{\nabla}\left(\vec{\nabla}.\vec{v}\right) \qquad (13b)$$

By depth integrating the horizontal component of the slowest terms, one obtains the component corresponding to the external mode $\left(\vec{\Lambda}_e\right)$ and to its internal-mode residue $\left(\vec{\Lambda}_i^{'}\right)$:

$$\vec{\Lambda}_e \equiv \begin{pmatrix} \left\langle \overline{\Lambda}_{i,x} \right\rangle_e \\ \left\langle \overline{\Lambda}_{i,y} \right\rangle_e \\ 0 \end{pmatrix} \text{ and } \vec{\Lambda}_i^{'} \equiv \vec{\Lambda}_i - \vec{\Lambda}_e \qquad (13c)$$

Relations (13c) express a common external / internal mode-splitting based on the momentum decomposition: $\rho\vec{v} = \overline{\rho\vec{v}} + \left(\rho\vec{v}\right)^{'}$. Under Boussinesq assumption this decomposition is applied to velocity not to momentum.

Relation (13b) makes the additional assumption that non-linear advective processes do not evolve at "very fast" time scales. This leads to linear acoustics but is fully relevant if we focus on non-hydrostatic processes.

The three-mode algorithm can then be implemented in two different ways: either with a realistic acoustic velocity (the algorithm is then in a "compressible configuration") or with a lower, unrealistic, acoustic velocity (we shall then talk about "pseudo-compressible configuration").

Time-steps for the NBQ, external and internal-modes are respectively written Δt_q, $\Delta t_e = N_q \Delta t_q$ and $\Delta t_i = N_e \Delta t_e$ recalling that $\Delta t_q \le \Delta t_e \le \Delta t_i$.

The three-mode algorithm is now discretized with a simple, low-order and well-known Leapfrog time-stepping. The advantages (simplicity, well-known treatment of the conservation of energy (Marsaleix et al., 2008) of this implementation together with its main drawbacks (stability only when associated to an Asselin-like time filter, optimal numerical properties under a reduced range of Courant numbers and phase-shift in the propagation of high-frequency waves) are known and well-documented (Lemarié et al., 2015). The present use of the Leapfrog scheme is thus to be viewed as a reference implementation which undoubtedly needs to be followed by a detailed analysis of a comparative analysis of higher-order space-time schemes.

3.2 Treatment of the continuity equation: conservation of mass

The full non-Boussinesq continuity equation (1b) is central to the three-mode algorithm. It enforces conservation of mass and, through its various formulations, it is used to prognosticate the surface elevation anomaly (Eq. 5), to compute the cross-σ vertical velocity (Appendices B and C) and it is at the root of the flux formulation of advection (Eq. B.4). It can also appear in the computation of the grid depth in σ-coordinates and more generality in s-coordinates.

The presentation of the algorithm is now restricted to (x, z) plane without loss of generality and the velocity is $\vec{v} = (u, w)$. The grid is supposed to move vertically at the internal-mode time-step and to remain steady during the integration of the NBQ-mode. Details of σ-grid implementation are given in Appendix B. The continuity equation can alternatively be reformulated in function of (w) after substitution of Relation (B3).

If (n_i, n_e, n_q) are the time-step indices for the internal, external and NBQ-modes, the fast, compressible, NBQ-mode can be written:

$$\{\rho u\}^{n_q+1} = \{\rho u\}^{n_q-1} + 2\Delta t_q \underbrace{\left(-c_s^2 \frac{\partial \delta\rho^{\,n_q}}{\partial x}\bigg|_z + \lambda \frac{\partial^2 \{\rho u\}^{n_q}}{\partial x^2} + \lambda \frac{\partial^2 \{\rho w\}^{n_q}}{\partial x \partial z} \right)}_{\equiv \Lambda_{nbq,x}^{n_q}} + 2\Delta t_q \left(\Lambda_e^{n_e} + \Lambda_{i,x}^{n_i} \right) \tag{14a}$$

$$\{\rho w\}^{n_q+1} = \{\rho w\}^{n_q-1} + 2\Delta t_q \underbrace{\left(-c_s^2 \frac{\partial \delta\rho^{\,n_q}}{\partial z} - \delta\rho^{\,n_q} g + \lambda \frac{\partial^2 \{\rho u\}^{n_q}}{\partial z \partial x} + \lambda \frac{\partial^2 \{\rho w\}^{n_q}}{\partial z^2} \right)}_{\equiv \Lambda_{nbq,z}^{n_q}} + 2\Delta t_q \Lambda_{i,z}^{n_i} \tag{14b}$$

$$\delta\rho^{n_q+1} = \delta\rho^{n_q-1} - 2\Delta t_q \left.\frac{\partial \rho_{bq}}{\partial t}\right|^{n_i} - 2\Delta t_q \left(\frac{\partial \{\rho u\}^{n_q}}{\partial x} + \frac{\partial \{\rho w\}^{n_q}}{\partial z} \right) \qquad (14c)$$

The system has been reduced to 3 equations with 3 unknowns by substituting the non-Boussinesq pressure anomaly by the non-Boussinesq density anomaly:

$$\delta p^{n_q} = c_s^2 \delta\rho^{n_q} \qquad (15)$$

Several choices have been made to end up with NBQ-system (14), the most significant being the use of ρ and $\{\rho\vec{v}\}$ as prognostic variables. The resulting system is linear in this couple of variables. Once again this choice is dictated by the necessity to end up with a discrete approximation of (14c) that is both conservative and accurate. This treatment is different from the approach proposed by Gatti-Bono and Colella (2006) to solve for the compressible Euler equations. Gatti-Bono and Colella indeed chose to decompose both the density (and thus pressure) and momentum fields. The divergence operator of the second-viscosity is additionally applied to the momentum and not to the velocity as in (13b) to optimize computations.

The linear operators which are necessary to compute the pressure force, the second-viscosity operator and the divergence of momentum in (14) are directly derived from the gradient and divergence matrices defined by Auclair et al. (2011) and are given in Appendix C in "σ"-coordinates. The originality of the approach proposed therein is to compute separately the matrices for the divergence and gradient operators. The Laplacian operator was then obtained by a matrix multiplication. This procedure permits a consistent discretization of the divergence and gradient matrices in terms of energy conservation and facilitates the formulation of the bottom, surface and lateral boundary conditions.

Linear equations (14a-b) can thus be reformulated in matrix-vector notations. The fluxes related to the second viscosity are linear and do not require the computation of any new operators.

The system of equations of the NBQ-mode is linear and an integration of the NBQ mode basically consists in three matrix-vector multiplications, two for the momentum equation (14a) and one for the continuity equation (14b).

3.3 External and internal modes

External and internal-modes are already discussed in Auclair et al. (2011) and only a short description is given hereafter. For surface-wave and more generally barotropic dynamics, the depth-integrated momentum and continuity equations can be formulated as:

$$\left\{\overline{\rho u}\right\}^{n_e+1} = \left\{\overline{\rho u}\right\}^{n_e-1} \underbrace{- 2\Delta t_e \rho_0 g \frac{\partial \zeta^{n_e}}{\partial x}}_{\equiv \Lambda_e^{n_e}} + 2\Delta t_e \left(\left\langle \overline{\Lambda}_{q,x} \right\rangle_e^{n_e} + \overline{\Lambda}_{i,x}^{n_i} \right) \qquad (16a)$$

$$\left\langle \rho_q \right\rangle^{n_e+1}\left(H+\zeta\right)^{n_e+1}=\left\langle \rho_q \right\rangle^{n_e-1}\left(H+\zeta\right)^{n_e-1}-2\Delta t_e\frac{\partial\left(H+\zeta\right)^{n_e}\left\{\overline{\rho u}\right\}^{n_e}}{\partial x} \qquad (16b)$$

where $\left\langle\ \right\rangle_e$ and hereafter $\left\langle\ \right\rangle_i$ stand for time-averages at respectively external and internal time-steps.

In equation (16b), the bottom topography and as a consequence the σ-coordinate grid (Appendix B) can additionally vary with the slow internal mode time-step (Appendix D and Auclair et al., 2014).

The "total" density ρ_q is the summation of the reference density with the Boussinesq low-frequency and non-Boussinesq anomalies: $\rho_q=\rho_0+\rho_{bq}+\delta\rho$. In this expression, the Boussinesq component is equal to its latest available value.

The low-frequency internal-mode system of equations is:

$$\left\{\rho u\right\}^{n_i+1}=\left\{\rho u\right\}^{n_i-1}\underbrace{+2\Delta t_i\left(-\rho_0 g\frac{\partial\zeta^{n_i}}{\partial x}-\frac{\partial}{\partial x}\int_z^{\zeta^{n_i}}\rho_{bq}^{n_i}gdz-\left.\frac{\partial u\left\{\rho u\right\}}{\partial x}\right|_i^{n_i}-\left.\frac{\partial w\left\{\rho u\right\}}{\partial z}\right|_i^{n_i}+\left.\delta F_{c,x}^{n_i}\right|_i+\nu\Delta\left\{\rho u\right\}_i^{n_i-1}\right)}_{\equiv\Lambda_{i,x}^{n_i}}$$

$$+2\Delta t_i\left\langle\Lambda_{q,x}\right\rangle_i^{n_i} \qquad (17a)$$

$$\left\{\rho w\right\}^{n_i+1}=\left\{\rho w\right\}^{n_i-1}\underbrace{+2\Delta t_i\left(\frac{\partial}{\partial z}\int_z^{\zeta^{n_i}}\rho_{bq}^{n_i}gdz-\left.\frac{\partial u\left\{\rho w\right\}}{\partial x}\right|_i^{n_i}-\left.\frac{\partial w\left\{\rho w\right\}}{\partial z}\right|_i^{n_i}+\left.\delta F_{c,z}^{n_i}\right|_i+\nu\Delta\left\{\rho w\right\}_i^{n_i-1}\right)}_{\equiv\Lambda_{i,z}^{n_i}}$$

$$+2\Delta t_i\left\langle\Lambda_{q,z}\right\rangle_i^{n_i} \qquad (17b)$$

$$\left.\frac{\partial\left\{\rho w\right\}_i}{\partial z}\right|_i^{n_i}=\left\langle-\frac{\partial\rho_q}{\partial t}\right\rangle_i^{n_i}-\left.\frac{\partial\left\{\rho u\right\}_i}{\partial x}\right|_i^{n_i} \qquad (17c)$$

$$\left\langle\rho_q\right\rangle_i^{n_i+1}\left(\theta^{n_i+1},S^{n_i+1}\right)=\left\langle\rho_q\right\rangle_i^{n_i-1}\left(\theta^{n_i-1},S^{n_i-1}\right)+2\Delta t\left(-\left.\frac{\partial\rho u\left(\theta,S\right)}{\partial x}\right|_i^{n_i+1}-\left.\frac{\partial\rho w\left(\theta,S\right)}{\partial z}\right|_i^{n_i+1}+\rho^{n_i}\left(\phi_\theta^{n_i},\phi_S^{n_i}\right)\right) \qquad (17d)$$

$$\rho_{bq}=\rho_{bq}\left(\theta,S,-\rho_0 gz\right) \qquad (17e)$$

Several differences need to be acknowledged between the present formulation of external and internal modes and their pressure-correction formulation proposed by Auclair et al. (2011):

- As momentum rather than velocity becomes the prognostic variable, both the external and internal modes need to be reformulated in terms of momentum. The velocity field might be needed by the NBQ algorithm

(to compute advective fluxes or in specific diffusion schemes) and it can then be calculated knowing the density $\langle \rho_q \rangle_i$.

- In the external mode, the iteration of the NBQ-mode at each external time-step provides an alternative to solve the cross-dependencies in traditional algorithms pointed out by Shcheptekin and McWilliams (2011). Indeed, the depth-average density $\overline{\langle \rho_q \rangle_e}$ is available when the external mode is integrated and more specifically when free-surface anomaly is prognosticated through (16b) whereas (model) σ-grid related variables are updated at internal time-step and are thus available in the NBQ mode. In the internal mode now, the continuity equation (17c) is only needed to calculate cross-σ vertical velocity w_σ.
- The non-hydrostatic component of the pressure force which appears in both the external and internal modes is given by the NBQ component of pressure. This component is indeed deduced from the corresponding component of density using the EOS (15) in the NBQ algorithm.
- Neither the free-surface anomaly nor the momentum have to be corrected in external or internal modes in the present NBQ algorithm whereas such correction is needed in pressure-correction methods. Indeed the continuity equation recovers its status of prognostic equation and is not a constraint any more. This is of considerable importance for the algorithm to be easily implemented with higher-order, mode complex but maybe more efficient time-stepping compared to Leap-Frog.

3.4 Three-mode time-splitting

Figure (1.a) shows the pressure-correction time-stepping used by Auclair et al. (2011). The NBQ time-stepping is represented in Figure (1b): the common Boussinesq external / internal mode-slitting algorithm is extended to include a third (NBQ) mode.

- *Step 1:* the external mode is integrated between t_i and $(t_i + \Delta t_i)$ with time-step Δt_e:
  - *Step 1a:* the NBQ mode is first integrated with time-step Δt_q from t_e to $t_e + \Delta t_e$ and $(\rho_q, \vec{\Lambda}_q)$ are time-averaged over $[t_e - \Delta t_e, t_e + \Delta t_e]$ to calculate their external-mode equivalent $(\langle \rho_q \rangle_e, \langle \vec{\Lambda}_q \rangle_e)$ at t_e.
  - *Step 1b:* the external mode is advanced from t_e to $t_e + \Delta t_e$.

    Both coupling terms $(\rho_q, \vec{\Lambda}_q)$ and $(\zeta_e, \{\overline{\rho \vec{v}}\}_e, \vec{\Lambda}_e)$, are time-averaged over $[t_i - \Delta t_i, t_i + \Delta t_i]$ to be used in the internal-mode. At this point, the complete solution at t_i is available.
- *Step 2:* an iteration of the internal mode is carried out between t_i and $(t_i + \Delta t_i)$.

After "Step 1", (total) density $\left(\rho_q\right)$ is available for both the external and internal modes (respectively through $\left\langle\overline{\rho_q}\right\rangle_e$ and $\left\langle\rho_q\right\rangle_i$). Variables are time-averaged when they are exchanged between the NBQ-mode and the external or internal-modes. Only the final value of the NBQ-component of density (in a Leapfrog formulation) is needed:

$$\left\langle\rho_q\right\rangle_i = \left\langle\rho_q\right\rangle_e = \frac{1}{2}\left(\rho_q^{t_q} + \rho_q^{t_q+\Delta t_q}\right) \qquad (18)$$

This is similar to the treatment of the free-surface anomaly which is computed in the external-mode and exchanged with the internal mode:

$$\left\langle\zeta_e\right\rangle_i = \frac{1}{2}\left(\zeta_e^{t_e} + \zeta_e^{t_e+\Delta t_e}\right) \qquad (19)$$

The RHS of the momentum equations are (Leapfrog) averaged when communicated from NBQ-mode to large time-step modes:

$$\left\langle\vec{\Lambda}_q\right\rangle_i = \frac{1}{4N_eN_q}\sum_{t_q=t_t-\Delta t_i+\Delta t_q}^{t_i+\Delta t_i}\vec{\Lambda}_q^{t_q} \qquad (20)$$

$$\left\langle\vec{\Lambda}_q\right\rangle_e = \frac{1}{2N_q}\sum_{t_q=t_e-\Delta t_e+\Delta t_q}^{t_e+\Delta t_e}\vec{\Lambda}_q^{t_q} \qquad (21)$$

The latest value is exchanged between external or internal modes and NBQ mode, indeed:

$$\left\langle\vec{\Lambda}_e\right\rangle_q^{n_q} = \vec{\Lambda}_e^{t_e=t_q} \quad \textit{and} \quad \left\langle\vec{\Lambda}_i\right\rangle_q^{n_q} = \vec{\Lambda}_i^{t_i=t_q} \qquad (22)$$

These filtering are clearly time-stepping dependent and the above averages are exclusively associated with the Leapfrog scheme.

3.5 Stability of the three-mode algorithm and pseudo-acoustic regime

The stability of the NBQ mode and an accurate representation of the induced non-hydrostatic processes by the external and internal modes are more important than an accurate representation of compressible processes.

The number of iterations N_q $\left(N_q = \Delta t_e / \Delta t_q\right)$ depends on the numerical properties of the linear system (14a) – (14c). This system describes the propagation and damping (due to second viscosity) of linear acoustic waves subject to slowly varying forcing: $\left\langle\vec{\Lambda}_e\right\rangle_q^{n_q}$ and $\left\langle\vec{\Lambda}_i\right\rangle_q^{n_q}$ at the RHS of momentum equations (14a) and (14b). The inviscid formulation is given and discussed in Appendix A (Eq. A5).

A simple unidirectional evaluation of the Courant number for acoustic waves is given by $Co_q \equiv c_s \Delta t_q / \Delta x$. This means that the time-step Δt_q depends on the space-time discretization and on the (pseudo-) acoustic wave velocity: the lower this velocity, the larger the time-step. The explicit damping due to the second viscosity can also lead to stability restrictions associated to the dedicated Courant number: $Co_\lambda \equiv \lambda \Delta t_q / \Delta x^2$. NBQ time-step Δt_q must be primarily chosen based on these simple stability criteria.

To minimize computational cost, the acoustic wave velocity (c_s) can be reduced and the new system of equations is not compressible any more but "pseudo-compressible". Stability is consequently enhanced since Courant number Co_q is proportional to c_s. A lower bound exists for the acoustic velocity and can be estimated on simple physical grounds. Acoustic waves have indeed been introduced in the three-mode algorithm in order to propagate pressure anomalies. If the velocity scale of the dynamical processes of interest is (much) slower than the acoustic wave velocity, these acoustic waves can propagate pressure anomalies with very few interactions, interferences or coupling with other dynamical processes. This must still be the case in the pseudo-acoustic regime which means that the pseudo-acoustic velocity must be "reasonably" larger than the velocity scale of the dynamical processes (say 5 to 10 times larger and less than real acoustic velocity). Here "reasonably" means here that incompressible dynamics must not be modified by any kind of spurious interactions, interferences or coupling. The lower bound for the acoustic velocity is thus associated to the fastest simulated processes. We can anticipate that the second viscosity reduces this coupling by limiting the amplitude of the acoustic waves (Section 4). In this case, the interactions, interferences and more generally the coupling between the fast NBQ (non-Boussinesq) mode and the external and internal modes do not disappear but their amplitude is reduced and their time-scale can be enhanced (Skamarock and Klemp, 1992). Such interactions or coupling can in particular occur due to the presence of the free-surface which can lead to specific acoustic modes. In terms of pressure, this means that surface-induced and non-hydrostatic pressure anomalies are correlated. As a consequence the implementation of the fast NBQ-mode in the external mode can lead to interactions requiring the reduction of the external mode time-step Δt_e. Let $\alpha_e \equiv \Delta t_e / \Delta t_{e,CFL}$ be the reduction coefficient where $\Delta t_{e,CFL}$ is the maximum external time-step associated to the Courant number for the propagation of the fast long surface waves $\left(Co_e \equiv \sqrt{gH}\Delta t_e / \Delta x\right)$. A situation with no acoustic coupling leads to $\alpha_e = 1$. When the surface-wave and (pseudo-) acoustic-wave velocities are separated by less than one order of magnitude, interactions can occur requiring a smaller coefficient α_e: the closer to each other the velocities, the smaller the coefficient. The likely interactions of the free-surface with the acoustic waves do not change the Courant number requirements for the (pseudo-) compressible modes.

4 Acoustic, surface and internal waves in ocean configurations

The ability of the complete three-mode non-Boussinesq algorithm to represent acoustic, surface and internal waves whether linear or not is now evaluated based on dedicated test configurations.

- Experiments A and B (Section 4.1) focus on the propagation and damping of acoustic waves.
- Experiment C (Section 4.2) focuses on the damping and dispersion of short-length scale surface-waves.
- Experiments D and E (Sections 4.3 and 4.4) focus on the generation, propagation, dispersion and damping of both linear and non-linear non-hydrostatic internal waves. Georges Bank configuration is in particular revisited and compared to the Boussinesq pressure-correction implementation proposed by Auclair et al. (2011), the idea being to evaluate the ability of the new algorithm to deal with complex topographies and complex dynamics.

In the remaining sections, Auclair et al. (2011)'s pressure-correction Boussinesq algorithm is called "NH" whereas the present non-Boussinesq algorithm is called "NBQ". When these algorithms are compared hereafter, the NH pressure-correction Poisson system is solved using HIPS[4] solver.

4.1 Acoustic waves

The propagation, damping and reflexion of acoustic waves are first investigated in two dedicated configurations.

4.1.1 Experiment A: spherical waves

A rather simple configuration of generation and propagation of acoustic waves is now presented in order to verify the primary characteristics of acoustic waves. Waves are generated by a high-frequency source of "sound" located at the centre of a 512 x 512 x 512 m closed domain. This source is represented as a forced harmonic oscillation of the NBQ-component of density $\delta\rho$. No stratification is imposed and the fields of salinity and temperature are chosen uniform. Currents and surface displacements are initialized to zero. In Experiment A, the phase-velocity of acoustic waves is constant and equal to 1500 ms^{-1}. Table 1 gathers the primary numerical parameters of the chosen configuration. CFL criteria related to acoustic waves and, to a smaller extend, surface gravity waves basically set the time-steps (Section 3.5). Dynamics is restricted to acoustic waves: their propagation and reflection on solid walls is simulated by the NBQ mode and their interaction with the free surface is given by both the external and NBQ modes. Consequently NBQ and external mode times-steps $\left(\Delta t_q = 0.1\text{ms} = \Delta t_e / 2\right)$ are chosen close to each other whereas internal mode time-

[4] http://hips.gforge.inria.fr/

step is two orders of magnitude larger. The implementation in the "acoustic configuration" is thus investigated in a 3D configuration with the complete three-mode algorithm.

Figure (2) shows a vertical section of the high-frequency density anomaly ($\delta\rho$). The propagation of spherical acoustic waves can be observed. The front of the wave is observed to move at 1500 m/s and its length scale is given by: $\lambda_0 = c_s T_0 = 1500 \text{x}\, 2.5 \text{x} 10^{-2} = 37.5 \text{m}$ in agreement with the linear theory of acoustic waves. In the absence of viscosity, the amplitude of the resulting 3D spherical acoustic wave can be shown to decrease as the inverse of the distance to the source (r) as its amplitude fits the analytical spherical wave $\left(\frac{A_0}{r} e^{-2\pi i (t/T_0 - r/\lambda_0)} \right)$ within 1.4 % (with a standard deviation of 3.7 10^{-2}) in the tank domain. Figure (2) shows reflections of the acoustic waves at the solid wall of the tank and at the free-surface as well.

3D acoustic waves can thus propagate in a dynamically coherent way with expected characteristics when compared to the linear theory of acoustic waves. The CFL criteria associated with their fast phase-velocity does not limit the internal mode time-step that can be chosen two-orders of magnitude larger $\left(\Delta t_i = 200 \Delta t_q\right)$.

4.1.2 Experiment B: acoustic wave filtering and reflexion in ocean configurations

In Experiment B, acoustic waves are generated by the oscillations of the bottom topography (Appendix D). Two configurations are studied (Figure 3): the first one (with high-frequency oscillations) focuses on the generation and propagation of small-scale acoustic waves (with vanishing surface waves), the second one (with lower-frequency oscillations) is dedicated to the generation of surface gravity waves (with non-vanishing acoustic waves) in an ocean-like configuration. Acoustic and surface-gravity waves are generated by an oscillating sine-shaped submarine mount of horizontal length-scale $\left(L_0\right)$. Numerical and physical parameters are presented in Table 2. Besides the frequency of the oscillations, these two configurations have different vertical-to-horizontal length-scale aspect ratio. This ratio is equal to 1 in the acoustic wave configuration whereas it is less than 1/10 in the ocean configuration. When not specified, the kinematic and second viscosities vanish in both configurations.

Figures (3a) and (3b) show a vertical section of the density anomaly $\left(\delta\rho\right)$ after 10 forcing periods $\left(0.1\text{s}\right)$. With a vanishing second-viscosity coefficient (Figure 3a), acoustic waves propagate obliquely from the oscillating mount toward the free surface (along black solid lines) before reflecting downward at the surface (along black dashed lines). The incident wave interferes with the reflected waves forming patterns of interferences. The black arrow above the surface shows the distance over which the acoustic wave is supposed to have propagated after 10 periods $\left(L_{AW} = c_s 10 T_1\right)$. The wave length-scale $\left(\lambda_1 = c_s T_1 \sim L_0\right)$ confirms that the wave is generated by the oscillating bathymetry. Figure (3b) presents a similar acoustic wave configuration but, this time, the second-viscosity coefficient does not vanish. Acoustic waves are damped compared to the previous configuration and the reflected waves have much lower amplitudes. Consequently the patterns of

interferences have small amplitudes and their extensions are spatially limited. The diffusion length-scale (λ_D) has the same order of magnitude as the depth.

Figures (3c) shows the same configuration but for typical "ocean scale ratios", i.e. for a small vertical to horizontal aspect ratio. In this case, the length scale of the acoustic waves generated by the oscillations of the bathymetry is large compared to the ocean depth: $\lambda_2 = c_s T_2 = 100\ \text{m} >> H_2 = 0.2\ \text{m}$ and the horizontal resolution $(\Delta x = 0.1\text{m})$ is of the same order of magnitude as the depth $(H < 0.2\ \text{m})$. A particularity of the proposed configuration is that the slope of the bathymetry is quasi-horizontal and the resulting acoustic waves propagate quasi-vertically. The resulting up-and-down quasi-vertical motion generates simple patterns of interferences with two maximum of vertical velocity in each column of water. These waves reflect alternatively at the surface and at the bottom of the ocean. They remain nearly invisible on Figure (3c) (solid and dashed arrow show the position of respectively ascending and descending waves).

4.2 Surface gravity waves

4.2.1 Experiment C: Natural oscillations of 10 x 10m tank

The surface oscillation of 10 x 10 m tank are now investigated in some details with the complete three-mode algorithm. Amplitude and phase errors of the surface oscillations are more specifically investigated when acoustic wave phase-velocity is varied in both compressible and "pseudo-compressible" configurations. The ability of the present algorithm to propagate short surface (gravity) waves is consequently evaluated in details. Following Chen (2003), the initial free surface anomaly is given by:

$$\zeta(x,t) = 10^{-3} \cos\left(\frac{\pi}{10} x\right) \qquad (23)$$

Tiny initial amplitudes (only 1 mm) are chosen to avoid the formation of non-linear bores during long integrations. For this simple configuration, linear, inviscid theory gives a period of natural oscillations of T_0 = 3.59 s. The primary numerical parameters of the experiments are given in Table 3.

With internal, external and compressible (NBQ) mode time-steps respectively equal to 0.482 s, 0.16 ms and 0.08 ms, amplitude error are both less than 1% of the analytical solution after 10 periods meaning that the numerical solution can hardly be distinguished from the analytical solution when plotted as a function of time (not shown).

With their pressure-correction algorithm and the same internal and external mode LeapFrog time-stepping, Auclair et al. (2011) uses an internal time-step equal to $3.21\ \text{ms}$ (for an equivalent grid) which is about 3 orders of magnitude smaller than the present internal time-step $\Delta t_i = 0.48\text{s}$. This is a consequence of the non-hydrostatic character of the small length-scale surface wave whose induced velocity is not constant over the water column. This z-dependence is simulated by the 3D NBQ-mode in the three-mode algorithm whereas with the pressure-correction method of Auclair et al. this imposes strong stability constraints to the internal

mode. A consequence is that the barotropic / baroclinic time-splitting remains attractive when implemented with the three-mode algorithm.

Experiment C can provide further insight into the consequences of a lowering the acoustic wave velocity on the damping and dispersion of surface gravity waves. Figure 4 compares the amplitude (4a) and phase (4b) of the oscillations after 50 periods with linear, inviscid theory. Amplitude and phase errors are expressed in percent of respectively the amplitude and phase of the analytical solution. Four sets of bars show the amplitude and phase errors when the velocity of pseudo-acoustic waves is varied. In order to vary as few parameters as possible, the NBQ time-step remains equal to half the external time-step. The external mode is replaced by the non-dimensional external mode coefficient α_e (let's recall that $\alpha_e = \Delta t_e / \Delta t_{e,CFL}$). A non-vanishing second viscosity is chosen for Set 2 only.

Figure 4 clearly shows the existence of a minimum phase velocity for acoustic waves: bellow this minimum velocity of about 40 ms^{-1} both the amplitude and phase errors drastically increase. This minimum velocity appears to be equal to 4 to 5 times the maximum velocity of the long surface gravity wave velocity (equal to 10 ms^{-1}). This can be explained by the physics of surface waves: the pressure disturbances need to be fast enough to propagate the surface-induced pressure anomalies over the water column. This is also confirmed by the fact that a reduction of the time-step by about 2 orders of magnitude between Set 1 and Set 4 does not reduce the errors with acoustic velocities lower than 40 ms^{-1}. For phase-velocities larger than 40 ms^{-1} now, amplitude and phase errors show a rather weak dependence on acoustic velocity but, as expected, they vary with α_e: the lower this ratio (and the time-steps), the lower the errors. When α_e is smaller than 0.05, amplitude and phase errors do not exceed a few percent.

When results of Sets 1 and 2 are compared, we can additionally observe that non-vanishing second viscosity damping greatly extents the domain of stability of the three-mode algorithm. This confirms that damping acoustic waves reduces the coupling with the free-surface. The individual stability of the NBQ mode (Section 3.5) is not problematic here: when not damped, acoustic waves can feed strong surface-acoustic modes that in turn impose strong Courant number limitations on the external time-step.

4.3 Linear internal tides in Ridge configuration (Experiment D)

Experiment D simulates the generation of linear internal gravity waves in a non-hydrostatic configuration. This experiment is adapted from Auclair et al. (2014) and it is similar to Experiment B: internal wave are generated in a closed tank by the oscillation of a ridge-like bathymetry simulating real ocean tidal oscillations. Auclair et al. compared the NH implementation to the measurements in the CNRM-GAME tank reaching the conclusion that their time-varying bathymetry algorithm was adapted to direct numerical simulations.

The primary dynamical and numerical parameters are given in Table (4, Tank configuration). External and NBQ-mode time-steps have the same order of magnitude ($\Delta t_q = 7.8410^{-3}\,\mathrm{ms} = \Delta t_e / 2$) but the internal-mode time-steps is two orders of magnitude larger $(\Delta t_i = 1.57\,\mathrm{ms})$ (like in the Experiments A and C). Internal mode time-step is given by (Mode 1) internal gravity-wave phase-velocity (see Table 4 for the time-step and

Courant number). Both External and NBQ-mode time-steps are given by high-frequency oscillations of bottom topography.

Figure (5) shows a vertical section of the Brunt-Väisälä frequency anomaly $\left(\Delta N^2\right)$. Internal wave rays can be observed in this "subcritical case" making an angle $\left(\theta \approx 42.5° \pm 0.5°\right)$ in agreement with the dispersion relation given by linear inviscid theory $\left(\sin\theta = 2\pi/(T_0 N_0)\right)$ where T_0 and N_0 are respectively the period of ridge oscillations and the Brunt-Väisälä frequency of the initial stratification (see Table 4, Tank configuration). Rays reflect at the surface and bottom of the water column and at lateral walls.

In this configuration dedicated to linear rays of internal waves, the consequences of lowering the acoustic wave velocity are now investigated. The RMS errors for the (u, w) velocity fields are presented in Figure (6). The RMS error is defined as the square root of the mean of the squares of the difference between a given implementation and the reference implementation. The Reference implementation is the NBQ configuration with a 1500 ms^{-1} acoustic wave phase-velocity (compressible configuration). High-velocity acoustic waves impose a small NBQ time-step (Δt_q = 7.8410^{-3} ms). Two sets of experiments have been carried out for NH and NBQ configurations: one using time-steps similar to those of the Reference configuration, the other with the largest possible time-steps. The principal parameters are presented in Table (4-Test configuration).

Figures (6a-d) show the RMS errors for NH and NBQ configurations relative to the Reference with pseudo-acoustic wave phase-velocities of 10, 20, 50 and 100 ms^{-1} (pseudo-compressible configuration). Figures (6a-b) show the RMS errors obtained when all the configurations are integrated with the same time-steps as the Reference simulation whereas RMS errors shown in Figures (6c-d) are obtained for configurations with optimal (larger) time-steps. Oscillations at half the forcing period can be observed and a quasi-stationary error level is reached after 3 to 4 periods.

With small time-steps equal to those of the Reference simulation, equivalent RMS errors (smaller than 10^{-3}) are obtained for NBQ configurations with acoustic velocities larger than 50 ms^{-1} and for the NH configuration. RMS errors for both components of velocity increase when the pseudo-acoustic wave phase-velocity is decreased, reaching RMS errors of 2.5 % for a phase-velocity of 10 ms^{-1}.

Two sets of optimal time-steps are shown in Figures (6c) and (6d) for the NH configurations: NH(o2) is integrated with an external mode time-step equal to half the time-step of the first configuration NH(o1). This latter configuration shows rather large RMS errors for both components of the velocity whereas the former NH(o2) presents levels of RMS errors at least one order of magnitude smaller, indicating a strong dependence to the time-step. For pseudo-acoustic wave velocities smaller than or equal to 20 ms^{-1}, RMS errors reach the same order of magnitude as NH(o1) and are approximately one order of magnitude larger than those obtained for pseudo-acoustic wave phase-velocities strictly larger than 20 ms^{-1}.

A conclusion from the present set of linear internal wave experiments is that provided pseudo-acoustic wave velocity larger than 20 ms^{-1} are specified, NBQ configurations show low levels of RMS errors with respect to the Reference (realistic) 1500-ms^{-1} implementation.

4.4 Non-linear internal waves: solitons

Two experiments of non linear internal waves are now investigated, both of them being presented in details in Auclair et al. (2011). Note that the pseudo-acoustic wave phase-velocity (4 ms^{-1}) is only 0.27 % of the realistic 1500 ms^{-1} phase-velocity. The first experiment (E) is a two-layer tank configuration selected among Horn et al. (2001)'s experiments, the second experiment (F) is a vertical section of internal tides in the region of Georges Bank similar to the experiment investigated by Lamb (1994).

4.4.1 Experiment E: Solitary waves in tank configuration

Table 5 gathers the primary physical and numerical parameters used to implement NH and NBQ configurations of 4 to 6 solitary waves corresponding to Horn et al. Regime 2 (their Figure (15.d)). Oscillations of the pycnocline are obtained by forcing a tilt at initial time-step. Figure (7) shows the resulting evolution in time of the depth of a middle-pycnocline isopycnal surface for NBQ (dashed line) and NH (solid line) models. In both implementations, a train of 6 solitary waves appears after 180 s, the number of solitary waves decreasing to 5 and than 4 solitons after a few reflections at the lateral solid walls and approximately 350 s of simulation.

Both the number of solitons and the arrival time of the train agree with experimental results described by Horn et al. (2001) and with the numerical results reported by Hodge et al. (2006, their Figure (3.12) corresponding to Scenario 3). Interestingly enough, NH and NBQ configurations do not present any clear discrepancies. A time bias of plus or minus two seconds can be observed in the NBQ implementation with respect to the NH implementation. No clear tendency can be highlighted for the amplitude of the oscillations of the pycnocline.

To conclude this first simulation of non-linear internal solitarity waves, NH and NBQ algorithms provide density fields in agreement with measurements in tank and with numerical models found in the literature.

4.4.2 Experiment F: Georges Bank solitary waves

A vertical section across Georges Bank (Gulf of Maine) is now investigated. Like Experiments C and E, the resulting configuration is similar to the configuration presented by Auclair et al. (2011) in order to facilitate comparisons between the NH and NBQ algorithms. The numerical configuration is similar to the configuration simulated numerically and analysed by Lamb (1994) as well. The numerical parameters are given in Table 6. M2 internal tide surface wave is introduced through the eastern (offshore) boundary condition, this wave can propagate across Georges Bank shelf break and it leaves the domain through the western shoreward open boundary. Note that slow internal-mode time-step was restricted by a few hot spots (locally high values of vertical-advection Courant number). The simulated vertical section allows the investigation of the large non-linear internal waves generated in the pycnocline region by strong tidal currents. These internal waves are observed propagating both shoreward and off-shore. They owe their non-linear character not only to the strength of tidal currents in the region but also to the steep slopes of the shelf break and to the moderate strength of the pycnocline. Cyclic transverse (cross-shore) open boundary

conditions permit the occurrence of along shore currents associated with Coriolis traditional pseudo-force. Solitary waves impose CFL criteria and consequently the internal mode time-step is similar to the time-step used in the NH pressure-correction configuration by Auclair et al. (2011).

Figure (8) shows a vertical section of the total density field after 1.625 tidal period (T_0) and should be compared with Auclair et al.'s Figure (5.a) and with Lamb's Figure (6.m). The three figures compare generally well. Solitary waves are generated by tidally induced motions above the shelf break and are propagating both shoreward and off shore. After 1.625 T_0, depressions A_1 and B_1 (generated during the first simulated tidal period) are located at respectively about 28 and 14 km from the shelf break. The location of depression (A_1) is approximately similar in the three simulations although the locations of depressions (B_1) differ by a few kilometres in these same numerical modelling studies. The shoreward most location is observed in Lamb experiment before NBQ and NH implementations.

Figures (9.a and 9.b) present cross-shore and vertical components of velocity after only one tidal period (T_0) and should now be compared with Lamb's Figures (7.a) and (7.b) and Auclair et al.'s Figures (5.a) and (5.b). The comparisons of the velocity components show close agreements between the three modelling studies. Minima and maxima of velocities have similar locations and their vertical structures are in close agreements. Amplitude of velocity anomaly whether shoreward or cross-shore are also similar.

As a conclusion, these results show that in this demanding ocean configuration, NBQ and NH implementations provide close and realistic high-frequency high-resolution ocean circulation, NBQ algorithm presenting density and velocity fields with amplitude ranging between those obtained by Lamb (1994) and Auclair et al. (2011).

5 Discussion, conclusion

Time-split approaches are currently used in weather forecast models (Skamarock and Klemp, 2008) to explicitly integrate sound waves with a smaller time-step. To our knowledge, the explicit simulation of such waves in free-surface ocean models based on a barotropic / baroclinic time-splitting is original.

Under the Boussinesq assumption, the mathematical degeneracy of the non-hydrostatic problem leads to the necessity to solve a large and, more importantly, global 3D Poisson system at each internal-mode time-step. No such system needs to be solved when acoustic waves are explicitly simulated with the three-mode time-splitting. A consequence is that surface-induced non-hydrostatic processes (such as short surface gravity waves) can be represented with the external and compressible (NBQ) modes exclusively imposing stability constraints on these two modes only. The internal-mode time-step can consequently be considerably increased compared to the pressure-correction method making the barotropic / baroclinic time-splitting in non-hydrostatic models particularly attractive. Since the details of the propagation of the acoustic waves are not of primary interest to simulate non-hydrostatic, incompressible, "slow" processes, the present study confirms that the velocity of the acoustic waves can be reduced to limit Courant-number restrictions.

Three wave configurations (surface-gravity, internal-gravity and acoustic waves) have been studied. In the former configuration (oscillations of the free surface) the physical coupling of the non-hydrostatic and surface-induced components of pressure appears as a key aspect of the three-mode free-surface algorithm. Errors on the amplitude and phase-shift of the surface oscillations have been shown to remain acceptable in pseudo-acoustic regimes as long as the acoustic wave velocity is larger than 5 times the velocity of long surface gravity waves.

Linear internal wave rays have then been studied in a moving-ridge (tank) configuration to evaluate RMS errors of the velocity field with respect to the (1500 ms^{-1}) acoustic wave configuration. Once again, as long as pseudo-acoustic wave velocity remains larger than both surface and internal wave velocities (i.e. faster than the fastest dynamical processes in the numerical domain), the amplitude of the RMS errors remains low reaching a stationary level after a few forcing periods. Non-linear configurations of internal waves and, in particular, solitary waves have been studied in a tank configuration and in a realistic, ocean-scale, configuration. In both cases, the three-mode algorithm compares well with similar analytical studies (Experiments A, B and C), with measurements in tanks (Experiments D and E), with in-situ observations (Experiment F) or with other modelling studies published in the literature (Experiments C, D, E and F).

In the present study, test cases show that the three-mode algorithm is well-adapted to parallel implementations although details are left to a future manuscript. The three-mode algorithm is also rooted in the Navier-Stokes equations and, as such, can be used in the future as a standard to evaluate new non-hydrostatic algorithms. Future studies should now assess the ability of the three-mode splitting algorithm to simulate compressible dynamics.

Acknowledgments: we gratefully thank the computer team of the *Laboratoire d'Aérologie* for "NUWA", our laboratory cluster, together with CALMIP (HYPERION) and CINES (JADE) for computer resources. The present study has been supported by the ANR projects PIWO (contract number ANR-08-BLAN-0113) and COMODO (ANR-11-MONU-005).

Appendix A: Consequences of the Boussinesq assumptions

(CSQ-i) Boussinesq momentum is approximated by $\rho\vec{v} \approx \rho_0\vec{v}$ (first order approximation with respect to the density anomaly) leading to an approximate conservation equation (6a).

(CSQ-ii) Neglecting the density anomalies with respect to a chosen reference state leads to an approximate form of the conservation of mass (6b). Once depth-integrated and combined with the unchanged kinematic conditions (3-4), the conservation of mass transforms into the conservation of the volume of the water column:

$$\frac{\partial(H+\zeta)}{\partial t} = -\frac{\partial(H+\zeta)\overline{v_x}}{\partial x} - \frac{\partial(H+\zeta)\overline{v_y}}{\partial y} \qquad (A1)$$

Another consequence of the approximation of the continuity equation (6b) through the Boussinesq assumption is the mathematical transformation of the resulting system of equations from a hyperbolic formulation to an elliptic formulation in terms of acoustic waves. Acoustic waves are supposed to propagate with an infinite velocity. The filtering of these fast, numerically demanding waves is justified by the Boussinesq approximation in large-scale and even in regional and coastal-scale ocean modelling.

(CSQ-iii) Continuity equation further loses its status of prognostic equation for density, a consequence being that Boussinesq momentum equations must be solved under the vanishing-divergence constraint (6b) whereas density can be diagnosed using the EOS. In hydrostatic Boussinesq models, vertical velocity is also usually diagnosed using the continuity equation and in non-hydrostatic Boussinesq models, this equation is a constraint for which pressure becomes the Lagrange multiplier (Salmon, 1998, p 313-315).

(CSQ-iv) The dependence of the density in the total pressure through the EOS cannot be maintained under the Boussinesq assumption leading to EOS (6d). The dependence in $(-\rho_0 gz)$ provides a "consistent Boussinesq energy conservation law" (Young, 2010) and Shchepetkin and McWilliams (2011) further show that a "stiffened" formulation is to be preferred to a more accurate formulation using the free-surface anomaly $(-\rho_0 g(\zeta - z))$ which can create a vertical shear in surface induced barotropic currents leading to cross-dependencies when barotropic / baroclinic mode-splitting is implemented.

(CSQ-v) Boussinesq assumption provides a consistent framework to study ocean dynamics in association with its own Bernoulli-like formulation of energy conservation (Young, 2010). A number of processes (in terms of ocean circulation) are excluded:

- bulk-compressibility processes such as acoustic waves (as already stated above their elimination is precisely one of the reasons of the popularity of the assumption),

- the steric effect is not excluded, it only has to be adjusted using the constraint on total ocean mass (Griffies and Greatbatch, 2012).
- dynamical processes related for instance to surface heating which can be crudely simulated whereas details are incorrectly depicted (Mellor and Ezer, 1995).

The linear propagation of (small amplitude) acoustic waves across a compressible, isentropic, inviscid, non-rotating, homogeneous $(\rho = \rho_0)$ ocean initially at rest satisfies a simplified version of Equations (1a-d):

$$\rho_0 \frac{\partial \delta\vec{v}}{\partial t} \approx -\vec{\nabla}\delta p \qquad (A2)$$

$$\frac{\partial \delta\rho}{\partial t} \approx -\rho_0 \vec{\nabla}.(\delta\vec{v}) \qquad (A3)$$

$$\delta p \approx c_s^2 \delta\rho \qquad (A4)$$

where gravity has been neglected and anomalies associated with the acoustic waves are written $(\delta\vec{v}, \delta p, \delta\rho)$. This leads to the following (hyperbolic) propagation equation for acoustic waves:

$$\frac{\partial^2 \delta p}{\partial t^2} - c_s^2 \Delta(\delta p) \approx 0 \quad \textit{(or equivalently } \frac{\partial^2 \delta\rho}{\partial t^2} - c_s^2 \Delta(\delta\rho) \approx 0 \textit{)} \qquad (A5)$$

Under the Boussinesq equation, (A3) degenerates to:

$$\vec{\nabla}.(\delta\vec{v}) \approx 0 \qquad (A6)$$

and pressure anomalies satisfy the elliptic equation:

$$\Delta(\delta p) \approx 0 \qquad (A7)$$

The computational cost of this large 3D linear system required by pressure projection and pressure correction methods must then be compared with the computational cost of high-frequency acoustic waves. Global systems potentially require a larger portion of global communications whereas local systems require communications with neighbours and are thus adapted to massively parallel implementation. Consequently, both the computational performances and the scalability of the resulting Boussinesq ocean model depend essentially on the performances of the Poisson solver implemented to calculate pressure increment. Non-Boussinesq dynamics is hyperbolic in terms of acoustic waves and it is consequently associated with severe CFL criteria for the computation of these high-velocity waves.

***Appendix B**: Non-Boussinesq system of equations in σ-coordinates*

The present version of the three-mode algorithm is implemented in σ-coordinates. The algorithm has no particular reason to be restricted to this particular vertical coordinates and can be formulated for any type of vertical coordinates. A formulation of the equations of the three-mode algorithm is given in the present appendix.

σ–coordinates can be introduced by writing:

$$z(x,y,\sigma;t)=\sigma\left[H(x,y,t)+\zeta(x,y,t)\right]-H(x,y,t)=\sigma\, h(x,y,t)-H(x,y,t) \qquad (B1)$$

where h is defined by $h\equiv\partial z/\partial\sigma$. At the surface ($z=\zeta$), $\sigma=1$ whereas, at the bottom ($z=-H$), σ vanishes. Model bathymetry (H) can further be made time-dependent (Auclair et al., 2014).

Momentum equations in σ-coordinates:

In σ-coordinates, the non-Boussinesq system of equations can be expressed in "flux form" as follows:

$$\left.\frac{\partial h\{\rho\vec{v}\}}{\partial t}\right|_\sigma=-h\vec{\nabla}_z^{(h)}p_h-h\vec{\nabla}_z\delta p+\delta\rho\, h\,\vec{g}-\mathrm{adv}\left(h\{\rho\vec{v}\}\right)+h\delta\vec{F}_c+\nu\Delta_\sigma h\{\rho\vec{v}\}+\lambda\vec{\nabla}\left(\vec{\nabla}.h\{\rho\vec{v}\}\right) \qquad (B2a)$$

$$\left.\frac{\partial h\rho}{\partial t}\right|_\sigma=\underbrace{-\left.\frac{\partial h\rho u}{\partial x}\right|_\sigma-\left.\frac{\partial h\rho v}{\partial y}\right|_\sigma-\frac{\partial\rho v_\sigma}{\partial\sigma}}_{-\mathrm{div}_\sigma\left(h\{\rho\vec{v}\}\right)} \qquad (B2b)$$

$$\left.\frac{\partial h\rho(\theta,S)}{\partial t}\right|_\sigma=-\frac{\partial hu\rho(\theta,S)}{\partial x}-\frac{\partial hv\rho(\theta,S)}{\partial y}-\frac{\partial\rho v_\sigma(\theta,S)}{\partial\sigma}+h\rho(\phi_\theta,\phi_S)h\rho \qquad (B2c)$$

$$\rho=\rho(\theta,S,p)=\rho_{bq}(\theta,S,-\rho_0 gz)+\underbrace{\left.\frac{\partial\rho}{\partial p}\right|_{\theta,S}\delta p}_{\delta\rho} \qquad (B2d)$$

where the divergence operator div_σ is $\mathrm{div}_\sigma\left(h\{\rho\vec{v}\}\right)=\left.\frac{\partial h\{\rho u\}}{\partial x}\right|_\sigma+\left.\frac{\partial h\{\rho v\}}{\partial y}\right|_\sigma+\frac{\partial\{\rho v_\sigma\}}{\partial\sigma}$. The vertical velocity across σ-surfaces $v_\sigma\equiv h\frac{d\sigma}{dt}$ is related to the vertical velocity w by:

$$w(x,y,\sigma;t)\equiv\frac{dz}{dt}=v_\sigma+\left.\frac{dz}{dt}\right|_\sigma=v_\sigma+\left.\frac{\partial z}{\partial t}\right|_\sigma+u\left.\frac{\partial z}{\partial x}\right|_\sigma+v\left.\frac{\partial z}{\partial y}\right|_\sigma=v_\sigma+\sigma\frac{d\zeta}{dt}+(\sigma-1)\frac{dH}{dt} \qquad (B3)$$

"σ"-subscribe indicates that the derivative is computed along "σ" surfaces. The newly defined vertical velocity v_σ vanishes both at the bottom and at the surface of the water column. The conservative formulation of the advection in σ -coordinates for momentum is:

$$\begin{aligned}\rho\frac{d\vec{v}}{dt}\Big|_z &= \frac{\partial\{\rho\vec{v}\}}{\partial t}\Big|_z + u\frac{\partial\{\rho\vec{v}\}}{\partial x}\Big|_z + v\frac{\partial\{\rho\vec{v}\}}{\partial y}\Big|_z + w\frac{\partial\{\rho\vec{v}\}}{\partial z} \\ &= \frac{1}{h}\left(\frac{\partial h\{\rho\vec{v}\}}{\partial t}\Big|_\sigma + \frac{\partial h\{\rho\vec{v}\}u}{\partial x}\Big|_\sigma + \frac{\partial h\{\rho\vec{v}\}v}{\partial y}\Big|_\sigma + \frac{\partial\{\rho\vec{v}\}v_\sigma}{\partial\sigma}\right)\end{aligned} \qquad \textit{(B4)}$$

Relation (B4) additionally defines the "flux advective" operator. To optimize computations, one needs another assumption in the present non-Boussinesq algorithm since in the momentum equations (B2a), the viscous diffusion operators are related to integrated momentum $\left(h\{\rho\vec{v}\}\right)$ not to velocity as they should.

A common difficulty of the formulation of non-hydrostatic models in σ-coordinates concerns the vertical velocity. Indeed, both the cross-σ $\left(v_\sigma\right)$ and true vertical $\left(w\right)$ velocities need to be computed, the latter with (B2a) whereas the former is a diagnostics based (for instance) on (B3).

Appendix C: *Space-discretization of the divergence and gradient operator*

To ensure correct energy transfers, the gradient operator (implemented in the non-hydrostatic pressure force) and the divergence operator (implemented in the continuity equation) cannot be treated independently. For readability, both operators are now expressed as functions of coefficients (α,β). These coefficients detailed in Appendix (C.3) are functions of the grid parameters and are given in the (x,z)-vertical layer.

C.1 Divergence operator

$k\in[1,k_{max}]$:

$$\left[\vec{\nabla}_\sigma.h\{\rho\vec{v}\}\right]_{i,k}=\frac{\left[h\{\rho u\}\right]_{i+\frac{1}{2},k}-\left[h\{\rho u\}\right]_{i-\frac{1}{2},k}}{\Delta x}+\{\rho w\}_{i,k+\frac{1}{2}}-\{\rho w\}_{i,k-\frac{1}{2}}-\left(\left[\left.\frac{\partial z}{\partial x}\right|_\sigma\{\rho u\}\right]_{i,k+\frac{1}{2}}-\left[\left.\frac{\partial z}{\partial x}\right|_\sigma\{\rho u\}\right]_{i,k-\frac{1}{2}}\right)$$

The space-discretization of the last terms (in brackets) is:

- Inner layers $(k\in]1,k_{max}[)$:

$$\left[\left.\frac{\partial z}{\partial x}\right|_\sigma\{\rho u\}\right]_{i,k+\frac{1}{2}}=\alpha_{i+\frac{1}{2},k+1}\{\rho u\}_{i+\frac{1}{2},k+1}+\beta_{i+\frac{1}{2},k}\{\rho u\}_{i+\frac{1}{2},k}+\alpha_{i-\frac{1}{2},k+1}\{\rho u\}_{i-\frac{1}{2},k+1}+\beta_{i-\frac{1}{2},k}\{\rho u\}_{i-\frac{1}{2},k}$$

- Surface layer $\left(k=k_{max}+\frac{1}{2}\right)$: $\left[\left.\frac{\partial z}{\partial x}\right|_\sigma\{\rho u\}\right]_{i,k_{max}+\frac{1}{2}}=\beta_{i+\frac{1}{2},k_{max}+\frac{1}{2}}\{\rho u\}_{i+\frac{1}{2},k_{max}+\frac{1}{2}}+\beta_{i-\frac{1}{2},k_{max}+\frac{1}{2}}\{\rho u\}_{i-\frac{1}{2},k_{max}+\frac{1}{2}}$

- Bottom layer $\left(k=\frac{1}{2}\right)$: $\left[\left.\frac{\partial z}{\partial x}\right|_\sigma\{\rho u\}\right]_{i,\frac{1}{2}}=\alpha_{i+\frac{1}{2},\frac{1}{2}}\{\rho u\}_{i+\frac{1}{2},\frac{1}{2}}+\alpha_{i-\frac{1}{2},\frac{1}{2}}\{\rho u\}_{i-\frac{1}{2},\frac{1}{2}}$

C.2 Non-hydrostatic pressure gradient operator

The gradient operator implemented in the non-hydrostatic pressure force is a first-order scheme similar to the one proposed by Auclair et al. (2011). It is written in the following for the non-Boussinesq pressure increment but is applied to the non-Boussinesq density increment in the NBQ-mode as the two variables are related by the linear EOS (B2d).

(i) Horizontal component $(k\in]1,k_{max}[)$: $\left.\frac{\partial\delta p}{\partial x}\right|_{z;i+\frac{1}{2},k}=\frac{\delta p_{i+1,k}-\delta p_{i,k}}{\Delta x}-\frac{z_{i+1,k}-z_{i,k}}{\Delta x}\left.\frac{\partial\delta p}{\partial z}\right|_{i+\frac{1}{2},k}$

The vertical pressure component at point $\left(i+\frac{1}{2},k\right)$ is given by:

- Inner layers $\left(k \in \left]1, k_{max}\right[\right)$:

$$\left.\frac{\partial \delta p}{\partial z}\right|_{i+1/2,k} = \frac{1}{4}\left(\frac{\delta p_{i+1,k+1} + \delta p_{i,k+1} - \delta p_{i+1,k} - \delta p_{i,k}}{\Delta z_{i,k+1/2}} + \frac{\delta p_{i+1,k} + \delta p_{i,k} - \delta p_{i+1,k-1} - \delta p_{i,k-1}}{\Delta z_{i,k-1/2}}\right)$$

- Surface layer $\left(k = k_{max} + \frac{1}{2}\right)$: $\left.\frac{\partial \delta p}{\partial z}\right|_{i+\frac{1}{2},k_{max}+\frac{1}{2}} = \frac{0 - \delta p_{i+1,k_{max}} - \delta p_{i,k_{max}}}{\Delta z_{i+\frac{1}{2},k_{max}+\frac{1}{2}}}$

(ii) Vertical component

- Inner layers $\left(k \in \left]1, k_{max}\right[\right)$: $\left.\frac{\partial \delta p}{\partial z}\right|_{i,k+1/2} = \frac{\delta p_{i,k+1} - \delta p_{i,k}}{\Delta z_{i,k+1/2}}$

- Surface layer $\left(k = k_{max} + 1/2\right)$: $\left.\frac{\partial \delta p}{\partial z}\right|_{i,k_{max}+\frac{1}{2}} = \frac{0 - \delta p_{i,k_{max}}}{\Delta z_{i,k_{max}+\frac{1}{2}}}$

C.3 (α, β)*-grid parameters*

- Inner layers :

$$k \in \left]1, k_{max}\right[: \alpha_{i+\frac{1}{2},k} = \frac{z_{i+1,k} - z_{i,k}}{4\Delta x}\frac{\Delta z_{i+\frac{1}{2},k}}{\Delta z_{i+\frac{1}{2},k-\frac{1}{2}}} = \frac{z_{i+1,k} - z_{i,k}}{4\Delta x}\frac{\Delta \sigma_{i+\frac{1}{2},k}}{\Delta \sigma_{i+\frac{1}{2},k-\frac{1}{2}}}$$

$$k \in \left[1, k_{max}\right[: \beta_{i+\frac{1}{2},k} = \frac{z_{i+1,k} - z_{i,k}}{4\Delta x}\frac{\Delta z_{i+\frac{1}{2},k}}{\Delta z_{i+\frac{1}{2},k+\frac{1}{2}}} = \frac{z_{i+1,k} - z_{i,k}}{4\Delta x}\frac{\Delta \sigma_{i+\frac{1}{2},k}}{\Delta \sigma_{i+\frac{1}{2},k+\frac{1}{2}}}$$

- Surface layer $\left(k = k_{max} + \frac{1}{2}\right)$: $\alpha_{i+\frac{1}{2},k_{max}+\frac{1}{2}} = \beta_{i+\frac{1}{2},\frac{1}{2}} = 0$ and $\beta_{i+\frac{1}{2},k_{max}+\frac{1}{2}} = \frac{\zeta_{i+1} - \zeta_i}{2\Delta x}$

- Bottom layer $\left(k = \frac{1}{2}\right)$: $\alpha_{i+\frac{1}{2},1} = \beta_{i+\frac{1}{2},k_{max}} = 0$ and $\alpha_{i+\frac{1}{2},\frac{1}{2}} = -\frac{H_{i+1} - H_i}{2\Delta x}$

Appendix D: *Time-varying bathymetry in Non-Boussinesq mode-splitting*

Auclair et al. (2014) show that bathymetry can be made time-varying with only few adaptations in a free-surface non-hydrostatic model. Its implementation in the new Non-Boussinesq mode-splitting algorithm is straightforward.

Model variable for surface anomaly is first replaced by the variations of the water column total depth (i.e. surface plus bathymetry). The surface pressure gradient and the vertical position of the model grid have then to be corrected from the motion of the bottom topography.

A specificity of Auclair et al. (2011)'s NH algorithm is the possibility to specify boundary conditions independently for the divergence $(\mathbf{D})$ and gradient $(\mathbf{M})$ operators before constructing the Laplacian operator $(\boldsymbol{\Delta} = \mathbf{DM})$. A direct consequence is that new bottom boundary conditions can be specified in terms of the horizontal and vertical components of the velocity. Identical matrix operators are used in the NBQ algorithm to compute the NBQ mode equations. Consequently, the NBQ boundary conditions associated with a varying bathymetry remains similar to those implemented in Auclair et al.'s NH algorithm:

$$u(z=-H)=u(\text{bathymetry}),\ w(z=-H)=w(\text{bathymetry}) \qquad (D1)$$

References

Auclair F., C. Estournel, J. Floor, M. Herrmann, C. N'Guyen and P. Marsaleix, 2011: A non-hydrostatic algorithm for free-surface ocean modelling. *Ocean Modelling.* 36, 49-70, doi:10.1016/j.ocemod.2010.09.006.

Auclair F., L. Bordois, Y. Dossmann, T. Duhaut, C. Estournel, J. Floor, P. Marsaleix, C. Nguyen, A. Paci and C. Ulses, 2014: Implementation of a time-dependant bathymetry in a free-surface ocean model. *Ocean Modelling.*, in press.

Blumberg A.F. and G.L. Mellor, 1987: "A Description of a Three-Dimensional Coastal Ocean Circulation Model", In: *Three-Dimensional Coastal Ocean Models, N. Heaps, Ed., 1-16, American Geophys. Union.*

Chen X.J., 2003: A fully hydrodynamic model for three-dimensional, free-surface flows. *International J. Num. Meth. Fluids.* 42: 929-952.

Chorin A., 1967: A Numerical Method for Solving Incompressible Viscous Flow Problems. *J. Comp Physics.* 2, 12-26.

Casulli V., 1999: A semi-implicit finite difference method for non-hydrostatic, free-surface flows. *International J. Num. Meth. Fluids.* 30: 425-440.

De Szoeke R.A. and R.M. Samelson, 2002: The duality between the Boussinesq and non-Boussinesq hydrostatic equations of motion. *Journal of Physical Oceanography,* Vol. 32, 2194-2203.

Dewar W.K., J. Schoonover, T.J. McDougall, W.R. Young, 2015: Semicompressible ocean dynamics. *Journal of Physical Oceanography.* Vol. 45, 149-157.

Dossmann Y., F. Auclair and A. Paci, 2013a: Topographically induced internal solitary waves in a pycnocline: primary generation and topographic control, *Phys. Fluids* 25 (066601).

Dossmann Y., F. Auclair and A. Paci, 2013b: Topographically induced internal solitary waves in a pycnocline: secondary generation and spatial selection criteria, *Phys. Fluids* 25 (086603).

Dukowicz J. K. and A. S. Dvinsky, 1992: Approximate Factorization as a High Order Splitting for the Implicit Incompressible Flow Equations. *Journal of Comput. Phys*. Vol. 102, Issue 2 336-347.

Durran D. R. and P. N. Blossey, 2012: Implict-Explicit Multistep Methods for Fast-Wave-Slow-Wave problems. *Monthly Weather Review.* Vol. 140. 1307-1325.

Gatti-Bono C. and P. Colella, 2006: An anelastic allspeed projection method for gravitationally stratified flows. *Journal of Comutational Physics,* 216, 589-615.

Gerkema t., J.T.F. Zimmerman, L.R.M. Maas and H. Van Haren, 2007: Geophysical and astrophysical dynamics beyond the traditional approximation. *Reviews of Geophysics,* 46.

Greatbatch R.J, Y. Lu and Y. Cai, 2001: Relaxing the Boussinesq approximation in ocean circulation models. *Journal of atmospheric and oceanic technology*, Vol. 18, 1911-1923.

Griffies, S.M., 2004: Fundamentals of Ocean Climate Models, vol. 496. *Princeton University Press*. 496 pp. ISBN-13#09780691118925.

Griffies, S. M., and R J Greatbatch, 2012: Physical processes that impact the evolution of global mean sea level in ocean climate models. *Ocean Modelling*, 51, DOI:10.1016/j.ocemod.2012.04.003.

Horn D.A., J. Imberger and G.N. Ivey, 2001: the degeneration of large-scale interfacial gravity waves in lakes. *J. Fluid Mech.*, Vol. 434, pp. 181-207.

Huang R.X. and Jin X., 2002: Sea surface elevation and bottom pressure anomalies due to thermohaline forcing. Part I: isolated perturbations. *Journal of Physical Oceanography*. Vol. 32, 2131-2151.

Janjic, Z.I., 2003: A Nonhydrostatic Model Based on a New Approach. *Meteorol. Atmos. Phys.*, 82, 271-285.

Lamb K.G., 1994 (L94): Numerical experiments of internal wave generation by strong tidal flow across a finite amplitude bank edge. *J. Geophys. Res.*, Vol. 99, NO. C1, 843-864.

Lamb K.G., 2004: nonlinear interaction among internal wae beams generated by tidal flow over supercritical topography. *Geophysical Research Letters*, Vol. 31.

Lemarié F., L. Debreu, G. Madec, J. Demange, J.M. Molines and M. Honnorat, 2015 : Stability constraints for oceanic numerical models : implications for the formulation of time and space discretizations. *Ocean Modelling*. 92, 124-148.

Mahadevan A., J. Oliger and R. Street, 1996: A non-hydrostatic mesoscale ocean model, part I: well-posedness and scaling. *J. Phys. Oceanogr.*, Vol. 26, 1868-1880.

Marsaleix P., F. Auclair, J. W. Floor, M. J. Herrmann, C. Estournel, I. Pairaud, C. Ulses, 2008: Energy conservation issues in sigma-coordinate free-surface ocean models. *Ocean Modelling*. Vol. 20, Issue 1, 61-89.

Marshall J., C. Hill, L. Perelman and A. Adcroft 1997: Hydrostatic, quasi-hydrostatic, and nonhydrostatic ocean modeling. *J. Geophys. Res.*, Vol. 102, NO. c3, 5733-5753.

Marshall J. and F. Scott, 1999: Open-ocean convection: observations, theory, and models. *Review of Geophysics, 37, 1, 1-64.*

Mellor, G.L., Ezer, 1995. Sea level variations induced by heating and cooling: An evaluation of the Boussinesq approximation in ocean models. *Journal of Geophysical Research* 100, 20557–20565.

Ogura Y. and N. A. Phillips, 1962: Scale analysis of deep and shallow convection in the atmosphere. *J. Atmos. Sci.*, 19, 173-179.

Salmon R., 1998: Lectures on geophysical fluid dynamics. *Oxford University Press. pp. 378.*

Shchepetkin, A. F. and J. C. McWilliams, 2011: Accurate Boussinesq oceanic modeling with a practical, ``stiffened'' equation of state. *Ocean Modeling*, **38**, pp. 41-70, doi:10.1016/j.ocemod.2011.01.010.

Skamarock W. C. And J. B. Klemp, 1992: The stability of time-split numerical methods for the hydrostatic and the nonhydrostatic elastic equations. *Monthly Weather Review.* Vol.120. 2109-2127.

Skamarock W. C. And J. B. Klemp, 2008: A time-split nonhydrostatic atmospheric model for weather research and forecasting applications. *Journal of Computational Physics.*. 227, 3465-3485.

Tailleux R., 2010: On the energetics of stratified turbulent mixing, irreversible thermodynamics, Boussinesq models and the ocean heat engine controversy. *Journal of Fluid Mechanics.I vol. 638, 339-382.*

Vallis G.K., 2006: Atmospheric and oceanic fluid dynamics. *Cambridge University Press*, 745p.

Young, W. R., 2010*:* Dynamic Enthalpy, Conservative Temperature, and the Seawater Boussinesq Approximation. *J. Phys. Oceanogr.*, 40, 394–400.

Figure Captions

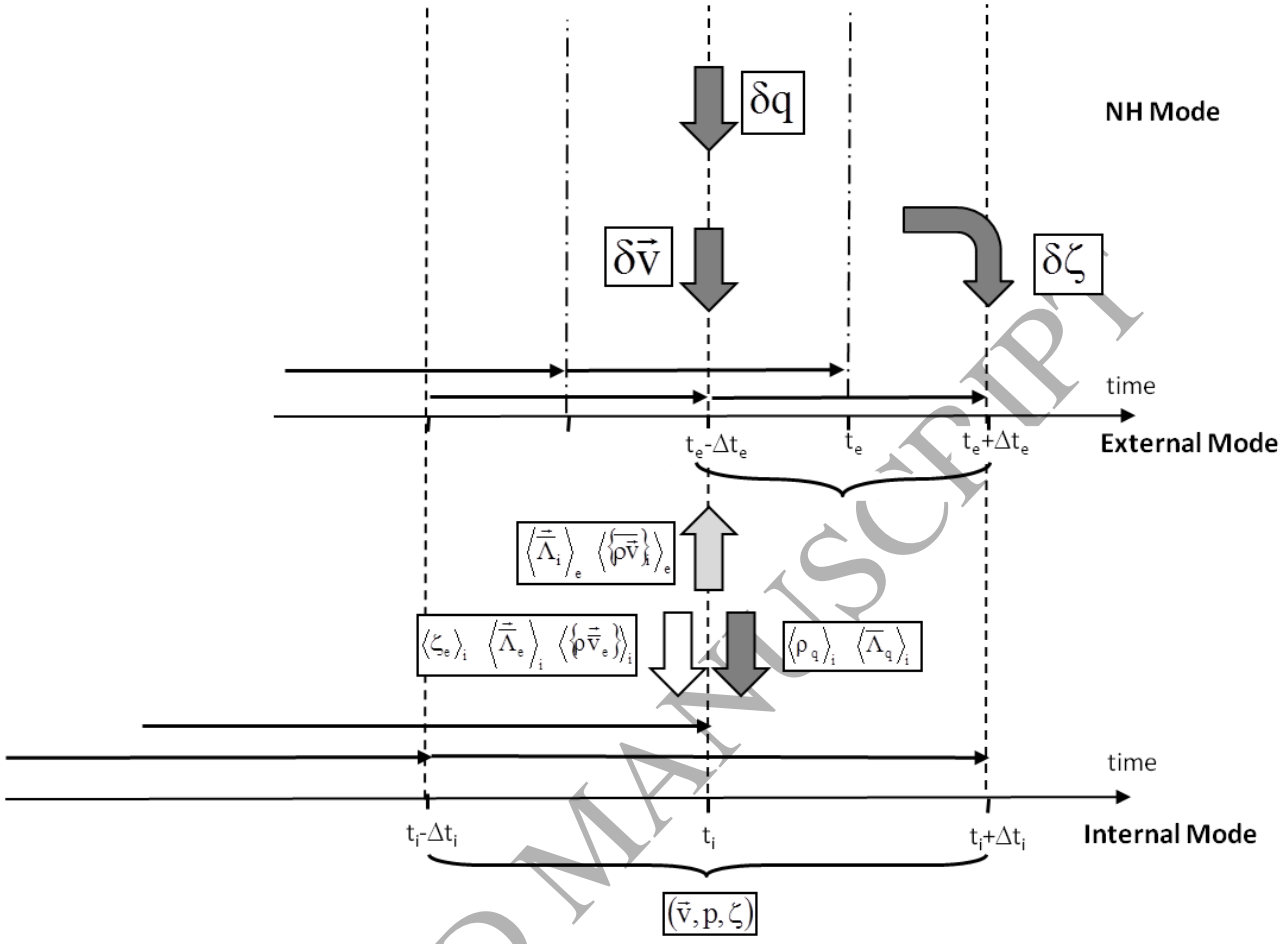

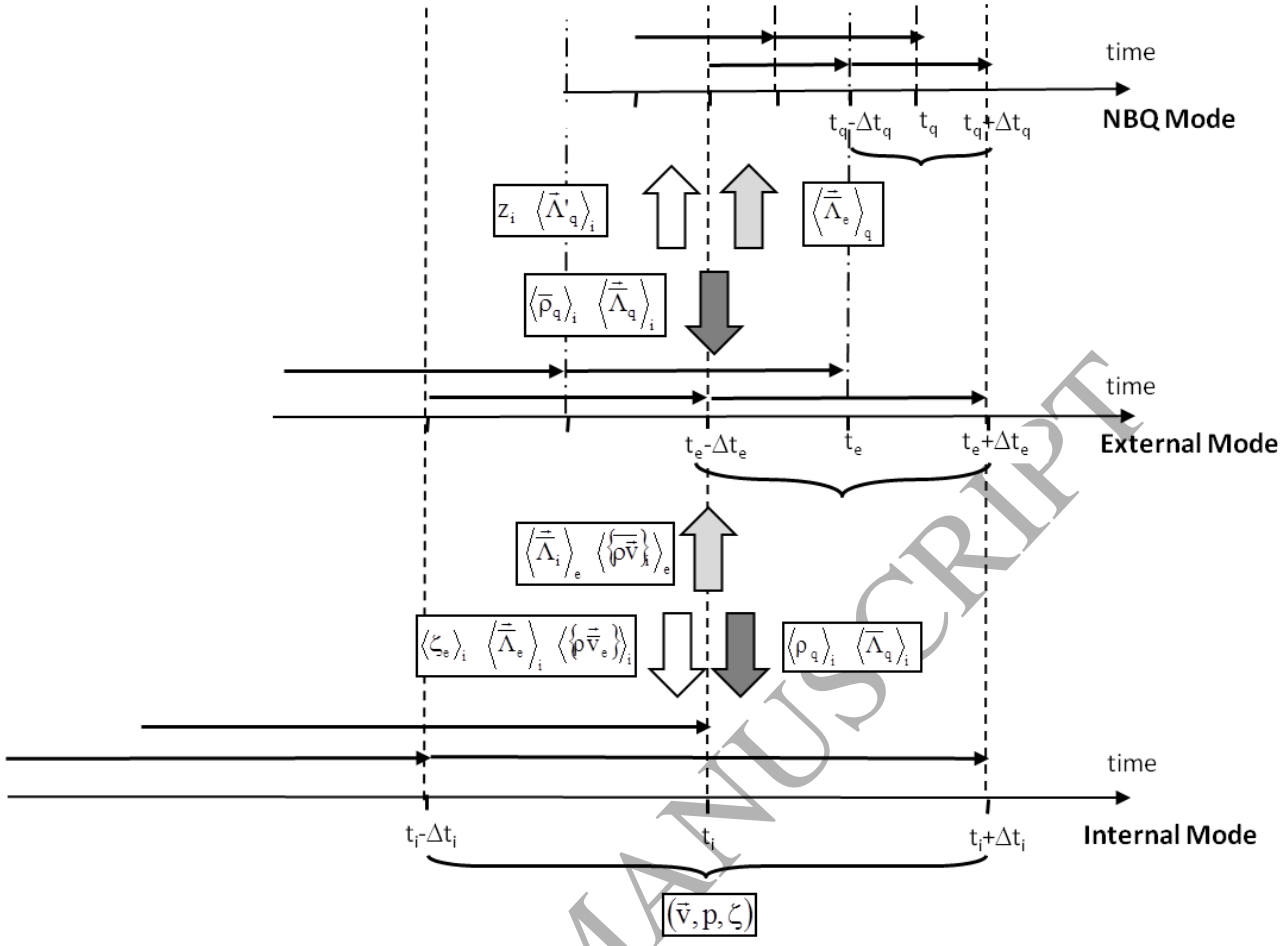

Figure 1: Schematic representation of NH (a) and NBQ (b) time-splitting algorithm. Yellow, blue and red colors are associated respectively with internal, external and NH / NBQ modes. Horizontal arrows represent Leapfrog evolution in time and remaining arrows indicate exchanges between the various modes and, consequently, the way they are updated.

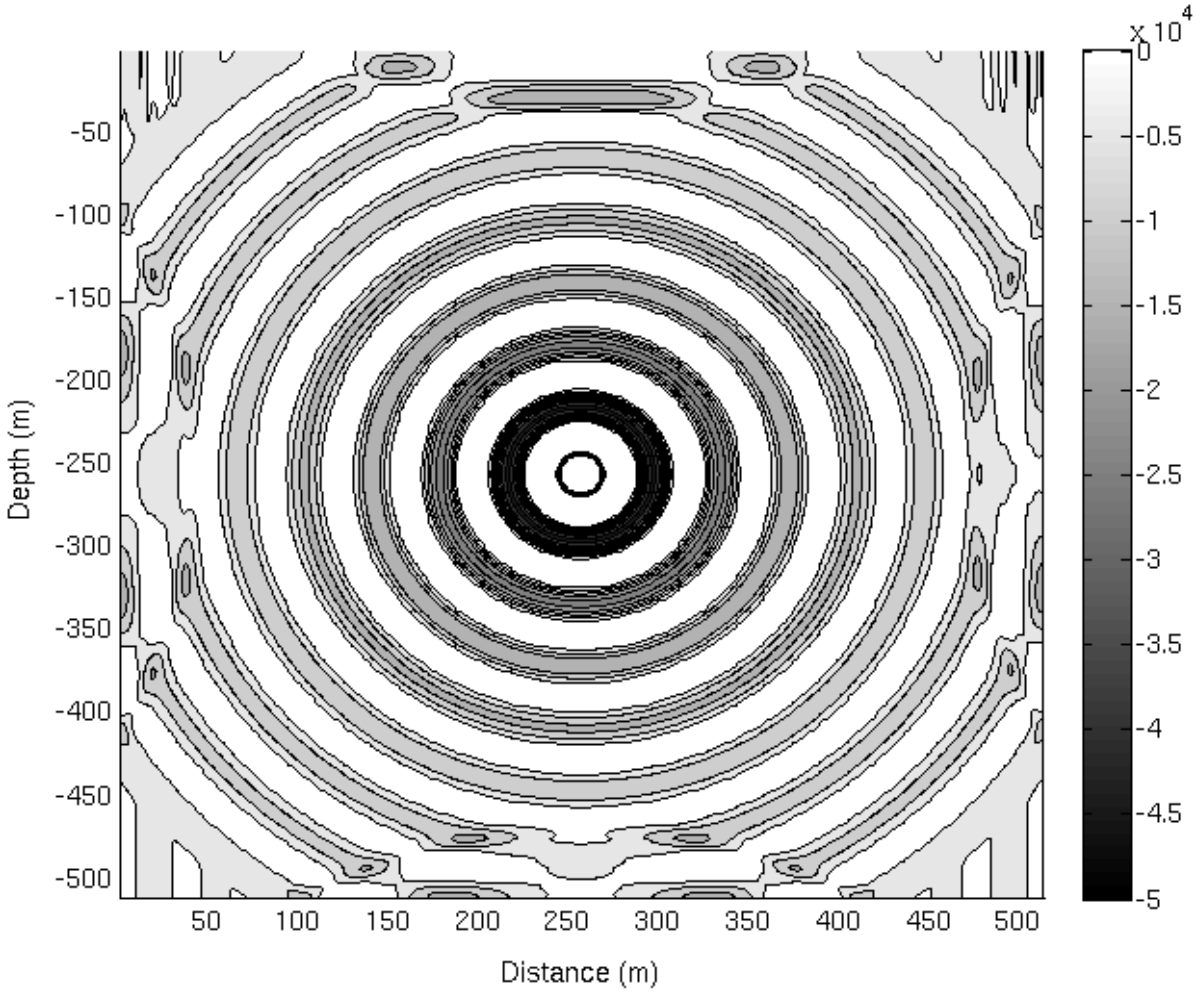

Figure 2: (Experiment A) Vertical section of density non-Boussinesq anomaly $(\delta\rho)$ in kg.m^{-3} after 20 s of acoustic forcing at the centre of the 3D domain. Distances are given in meters.

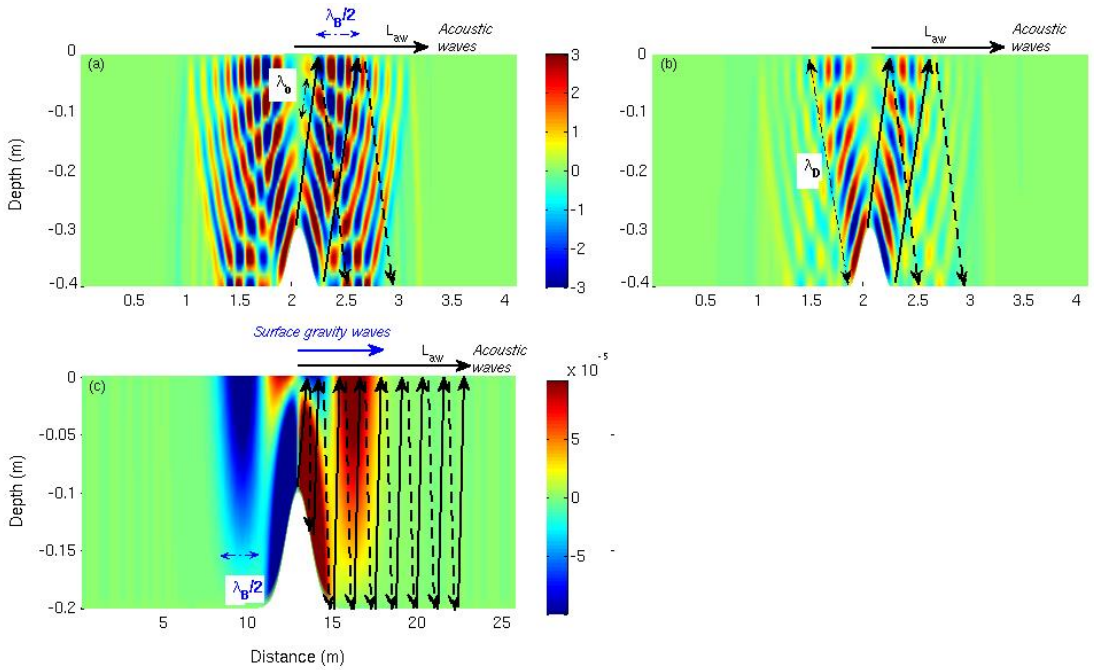

Figure 3: (Experiment B): Vertical section of density anomalies (a and b) after 80 ms in $kg.m^{-3}$ and of vertical velocity (c) after 2.5 s in $m.s^{-1}$. (a) Acoustic configuration with a vanishing second-viscosity. (b) Acoustic configuration with a non-vanishing second-viscosity. (c) Ocean-like configuration. Black arrows: direction of propagation of acoustic waves (solid lines) and downward propagating reflected acoustic waves (dashed lines). Blue arrows: direction of propagation of surface gravity waves.

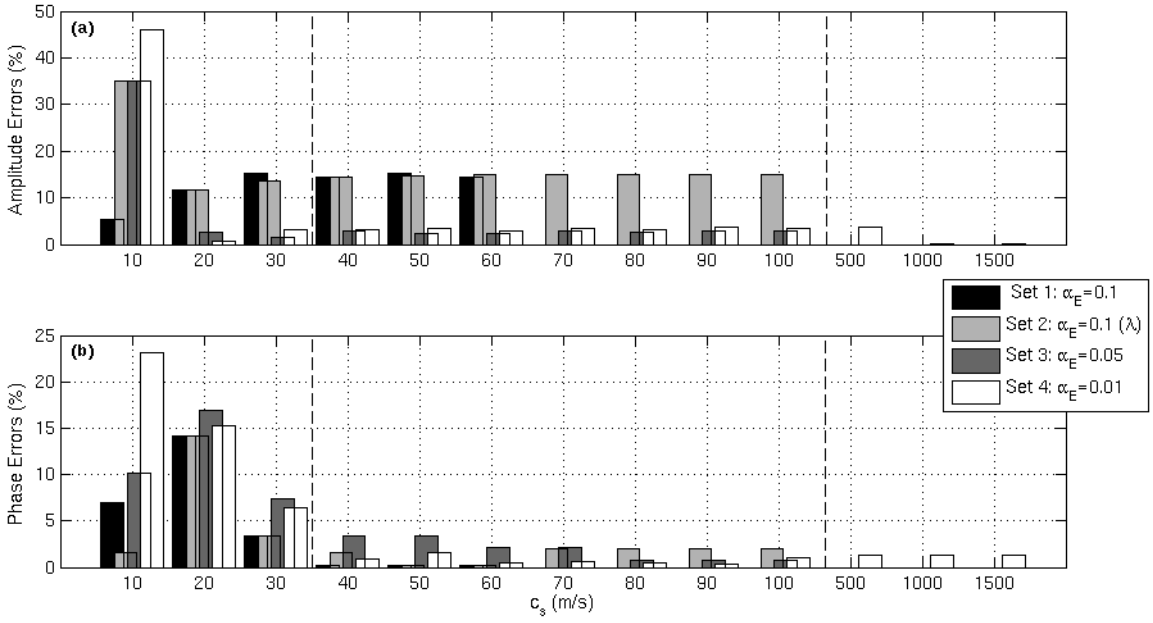

Figure 4: (Experiment C) Amplitude (a) and phase (b) errors with respect to linear inviscid theory as functions of the wave phase-velocity in ms^{-1} after 50 natural oscillation periods. Bar colors indicates the set of experiments obtained for different external mode coefficients: Set 1: $\alpha_e = 0.1$, Set 2: $\alpha_e = 0.1$ and

$\lambda = 1\ \mathrm{m^2 s^{-1}}$, Set 3: $\alpha_e = 0.05$, Set 4: $\alpha_e = 0.01$. Errors are given in percent of the initial amplitude (a) and of the natural oscillation period (b).

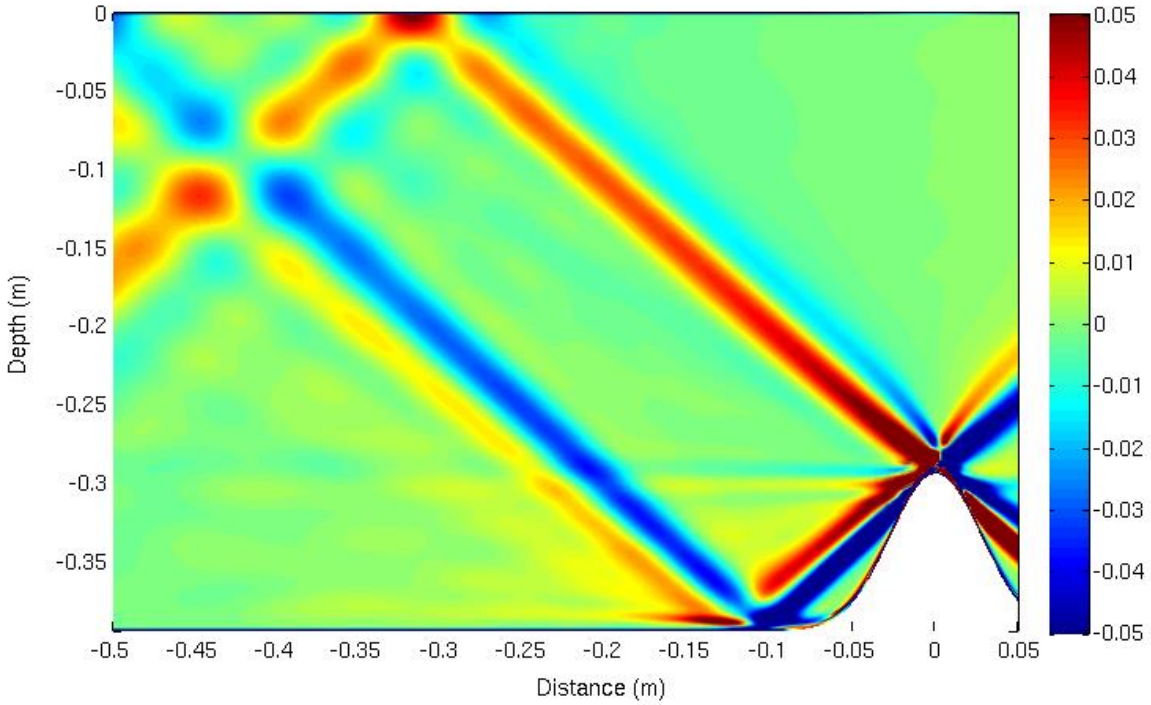

Figure 5: (Experiment D) Vertical section of square Brunt-Väisälä pulsation anomaly ($\mathrm{rad^2 s^{-2}}$) after 10 forcing periods simulated numerically with NBQ algorithm. This Figure can be compared with Auclair et al. (2014)'s Figure 1. They plotted the same vertical section of square Brunt-Väisälä pulsation anomaly (a) measured by Synthetic Schlieren and (b) simulated numerically with NH algorithm.

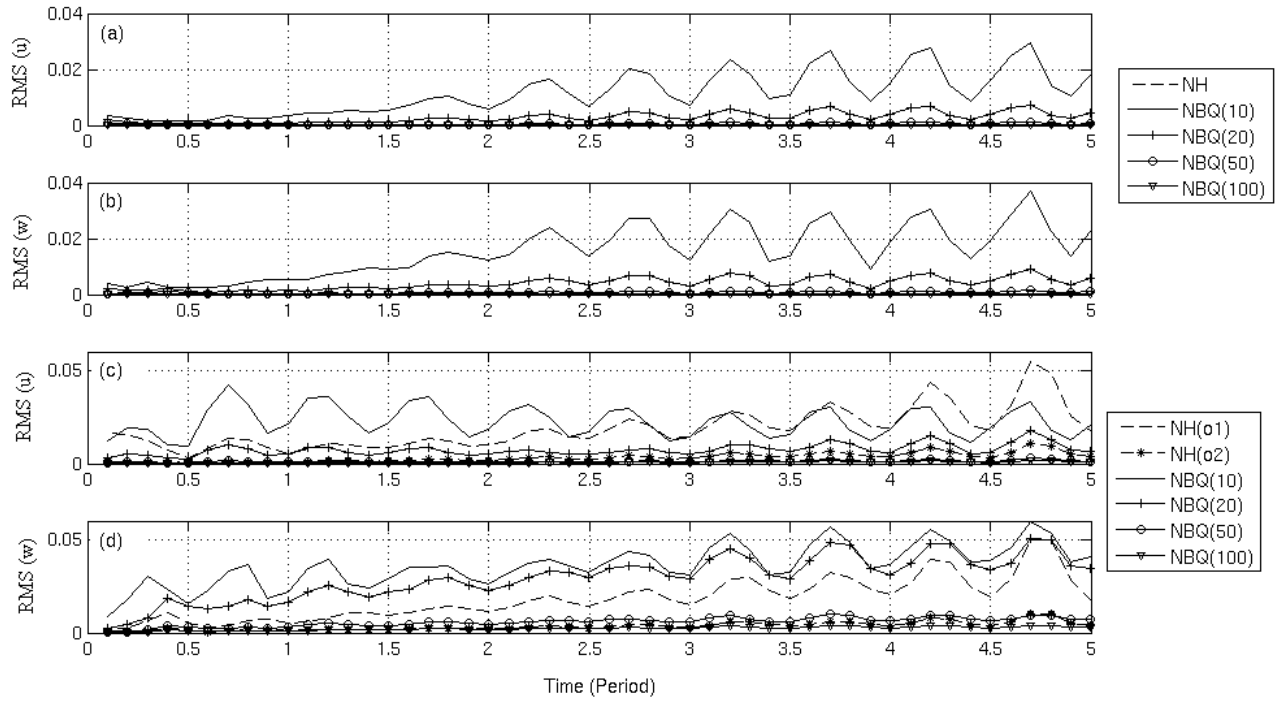

Figure 6: (Experiment D) RMS errors (%) of horizontal (a, c) and vertical (b, d) velocity components during the first 5 forcing periods for small (1500 m.s^{-1} phase-velocity) time-steps (a, b) and optimally adjusted time-steps (b, d).

(a, c): RMS errors (%) are plotted for NH configuration (dashed line), 10 ms^{-1} (solid line), 20 ms^{-1} (solid line and + signs), 50 ms^{-1} (solid line and diamonds) and 100 ms^{-1} (solid line and lower triangle) phase-velocity NBQ configurations.

(b, d): RMS errors (%) are plotted for NH configurations (dashed line for Set (o1) of optimal parameters and dashed line and * for Set (o2) of optimal parameters), 10 ms^{-1} (solid line), 20 ms^{-1} (solid line and + signs), 50 ms^{-1} (solid line and diamonds) and 100 ms^{-1} (solid line and lower triangle) phase-velocity NBQ configurations.

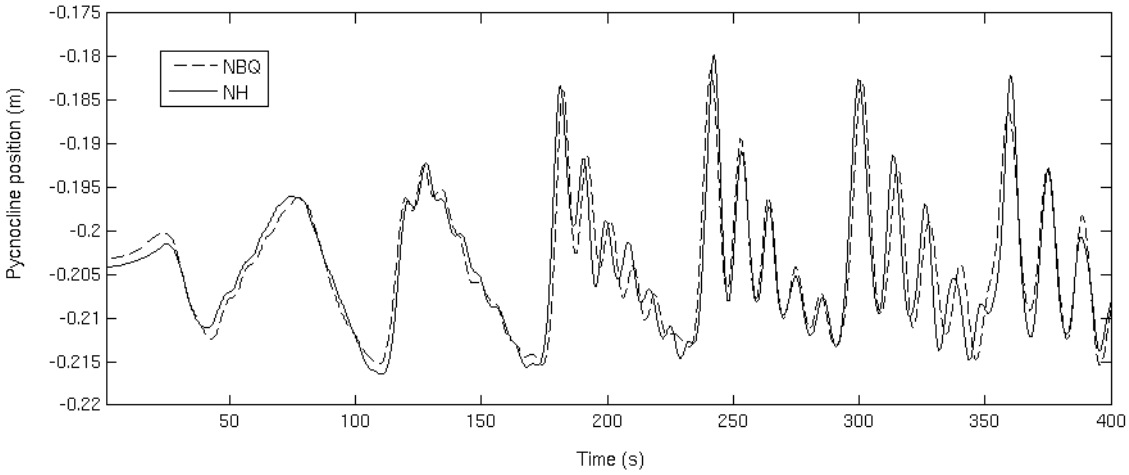

Figure 7: (Experiment E) Depth of the mid-pycnocline isopycnal surface in meters as a function of time (in second). (Dashed line): NH configuration, (Solid line): NBQ configuration.

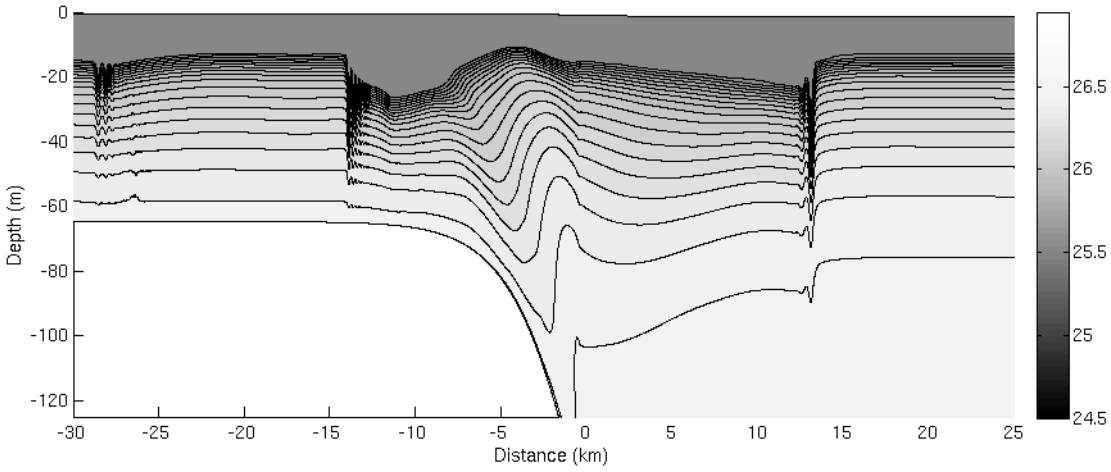

Figure 8: (Experiment F) Vertical sections of the total density anomaly in kg.m^{-3}. Horizontal distances are given en km and depths in meters.

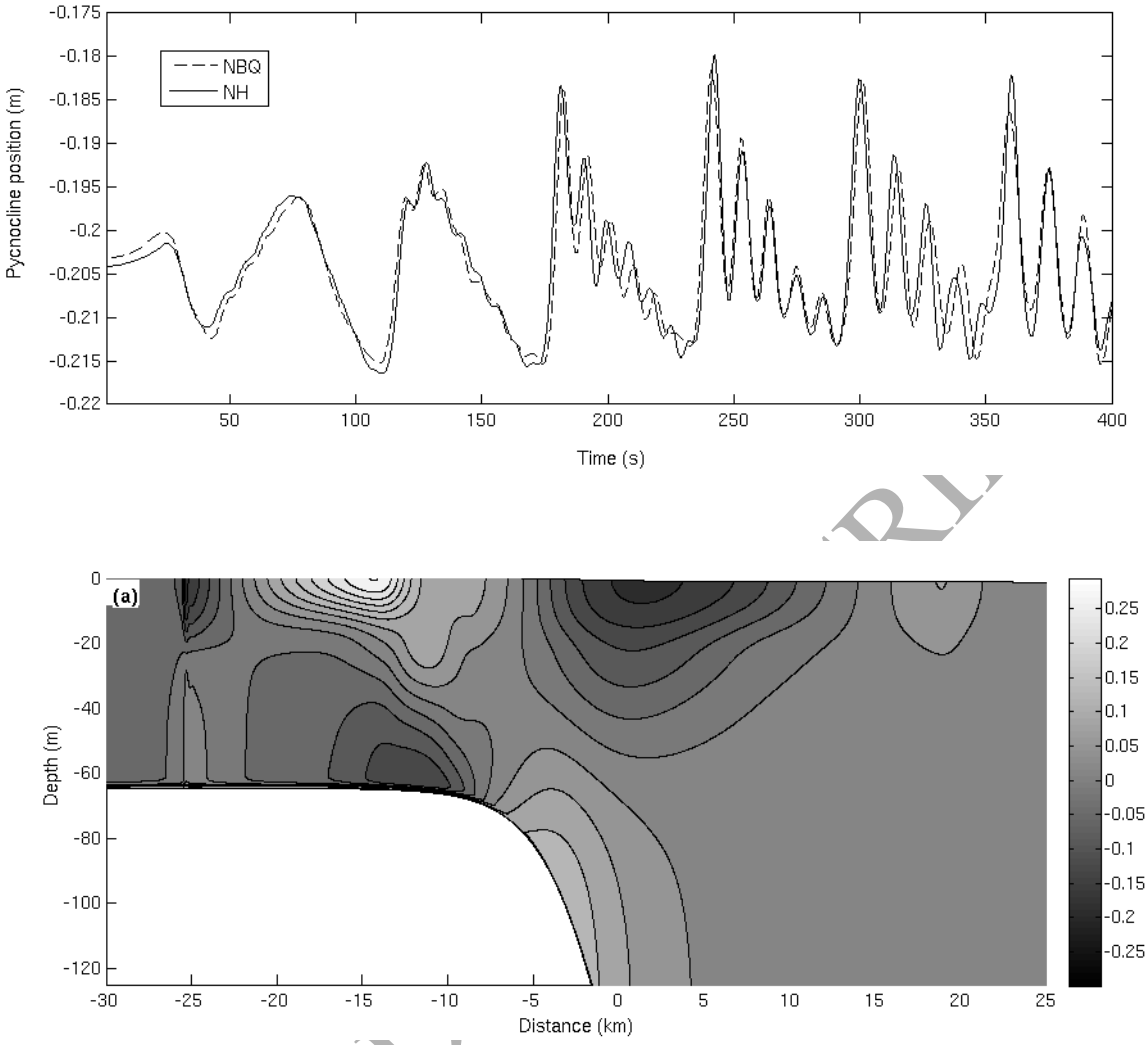

Figure 9: (Experiment F) Vertical sections of cross-shore (a) and vertical (b) components of the velocity (ms^{-1}). Horizontal distances are given en km and depths in meters.

Tables

Size of the domain (m)	(L_I, L_J, h_{max})	(512, 512, 512)
Number of points of model grid in x, and y direction.	(i_{max}, j_{max})	(512, 512)
Horizontal model grid (m)	$\Delta x = \Delta y$	1
σ -levels	k_{max}	512 equally-spaced levels
Total simulation time (s)		20
Internal mode time step (ms)	Δt_i	22
External mode time step (ms)	Δt_e	0.22
Compressible mode time step (ms)	Δt_q	0.11
Acoustic Courant number	Co_q	0.165
Phase-velocity of pseudo-acoustic waves (ms^{-1})	c_s	1500
Kinematic viscosity ($m^2.s^{-1}$)	ν	0.
Second viscosity ($m^2.s^{-1}$)	λ	0.
Asselin Filter Parameter		10^{-3}
Diffusivity ($m^2.s^{-1}$)	K_D	0.
Amplitude ($kg.m^{-3}.s^{-1}$), e-folding (m) and period of forcing (ms)	(A_0, L_0, T_0)	(1000, 2.5, 25)

Table 1: Primary characteristics of Experiment A.

		Acoustic configuration	Ocean-like configuration
Size of the tank (m)	(L_I, h_{max})	(4.1 , 0.4)	(25.6 , 0.2)
Number of points of model grid in x and y direction.	(i_{max}, j_{max})	(4096, 1)	(256, 1)
Horizontal model grid (m)	$\Delta x = \Delta y$	10^{-3}	0.1
σ -levels	k_{max}	40 equally-spaced levels	20 equally-spaced levels
Mount Height (m)	h_0	0.1	0.1
Mount horizontal scale (m)	L_0	(Sine-shaped mount) 0.4	(Gaussian-shaped mount) 1
Gaussian Mount Oscillations Amplitude (m) / Period (s)	(A_0, T_0)	$(10^{-4}, 10^{-2})$	$(10^{-2}, 10)$
Total simulation time (s)		2.5	2.5
Internal mode time step (ms)	Δt_i	$6.2\ 10^{-2}$	4.3
External mode time step (ms)	Δt_e	$3.1\ 10^{-2}$	0.43
NBQ mode time step (ms)	Δt_q	$1.6\ 10^{-2}$	0.22
Acoustic Courant number	Co_q (horizontal, vertical)	(0.16, 0.16)	(0.02, 0.22)
Phase-velocity of pseudo-acoustic waves (ms^{-1})	c_s	10	10
Kinematic viscosity ($m^2.s^{-1}$)	ν	0	0
Second viscosity ($m^2.s^{-1}$)	λ	$0 / 10^{-2}$	0
Asselin Filter Parameter		10^{-3}	10^{-3}
Diffusivity ($m^2.s^{-1}$)	K_D	10^{-9}	10^{-9}

Table 2: Model parameters for Experiment B in acoustic and ocean-like configurations.

Size of the tank (m)	(L_I, h_{max})	(10 , 10)
Number of grid points of model grid in x and y direction.	(i_{max}, j_{max})	(100, 1)
Horizontal model grid (m)	$\Delta x = \Delta y$	0.1
σ -levels	k_{max}	100 equally-spaced levels
Total simulation time (s)		180
Internal mode time step (ms)	Δt_i	*Set 1 & 2:* 642 *Set 3:* 482 *Set 4:* 96
External mode time step (ms)	Δt_e	*Set 1 & 2:* 0.32 *Set 3:* 0.16 *Set 4:* 0.032
NBQ mode time step (ms)	Δt_q	*CFL requirements (Section 3.5): up to 0.16 ms*
Surface gravity-wave Courant number	Co_e	*Set 1 & 2:* 0.032 *Set 3:* 0.016 *Set 4:* 0.0032
Phase-velocity of pseudo-acoustic waves (ms^{-1})	c_s	40
Equation of state		Compressible
Kinematic viscosity ($m^2.s^{-1}$)	ν	10^{-7}
Second viscosity ($m^2.s^{-1}$)	λ	0 or 1
Asselin Filter Parameter		10^{-2}

Table 3: Model parameters for Experiment C.

		Tank configuration	Test configurations
Size of the tank (m)	(L_I, h_{max})	(4 , 0.394)	(1 , 0.2)
Number of points of model grid in x and y direction.	(i_{max}, j_{max})	(4096, 1)	(256, 1)
Horizontal model grid (m)	$\Delta x = \Delta y$	10^{-3}	$4\ 10^{-3}$
σ -levels	k_{max}	400 equally-spaced levels	100 equally-spaced levels
Gaussian Mount Height (m)	h_0	0.1	0.05
Gaussian Mount horizontal scale (m)	L_0	$3.86\ 10^{-2}$	$3.86\ 10^{-2}$
Gaussian Mount Oscillations Amplitude (m) / Period (s)	(A_0 , T_0)	$(10^{-3} , 10.05)$	$(10^{-3} , 10)$
Brunt-Väisälä pulsation ($rad.s^{-1}$)	N	0.92461	1
Total simulation time (s)		50.25	50.25
Internal mode time step (ms)	Δt_i	1.57	3.46
External mode time step (ms)	Δt_e	$1.57\ 10^{-2}$	$8.67\ 10^{-4}$
NBQ mode time step (ms)	Δt_q	7.8410^{-3}	$4.34\ 10^{-4}$
Internal wave Courant number (for Mode 1 internal waves)	Co_{iw}	0.2	0.2
Phase-velocity of pseudo-acoustic waves (ms^{-1})	c_s	10	100 / 50 / 20 / 10
Equation of state (16)		Linear	Linear
Kinematic viscosity ($m^2.s^{-1}$)	ν	10^{-6}	10^{-6}
Second viscosity ($m^2.s^{-1}$)	λ	10^{-3}	10^{-4}
Asselin Filter Parameter		10^{-3}	10^{-5}
Diffusivity ($m^2.s^{-1}$)	K_D	10^{-9}	10^{-9}

Table 4: Model parameters for Experiment D in tank configuration (Auclair et al., 2014) and Test configurations.

Size of the tank (m)	(L_I, h_{max})	(6, 0.29)
Number of points of model grid in x and y direction.	(i_{max}, j_{max})	(60, 1)
Horizontal model grid (m)	$\Delta x = \Delta y$	0.1
σ -levels	k_{max}	74 equally-spaced levels
Internal mode time step (ms)	Δt_i	*NBQ:* 37.4 *NH:* 37.4
Total simulation time (s)		400
External mode time step (ms)	Δt_e	*NBQ:* 0.934 *NH:* 18.7
NBQ mode time step (ms)	Δt_q	*NBQ:* 0.093 *NH:* -
Two-layer density difference ($kg.m^{-3}$)	$\Delta\rho$	20
Horn's parameter	Δ	0.45
Horn's parameter	γ	0.3
Phase-velocity of pseudo-acoustic waves (ms^{-1})	c_s	4
Equation of state (16)		Linear
Kinematic viscosity ($m^2.s^{-1}$)	ν	10^{-6}
Second viscosity ($m^2.s^{-1}$)	λ	0.1
Asselin Filter Parameter		*NBQ:* 0.1 *NH:* 0.3
Diffusivity ($m^2.s^{-1}$)	K_D	10^{-7}

Table 5: Model parameters for Experiment E.

Size of the domain (m)		(67500, 45, 260)
Number of points of model grid in x and y direction.	(i_{max}, j_{max})	(4500, 3) Cyclic boundary conditions in y-direction.
Horizontal model grid (m)	$\Delta x = \Delta y$	15
σ -levels	k_{max}	100 equally-spaced levels
Total simulation time (day)		1
Internal mode time step (ms)	Δt_i	458.1
External mode time step (ms)	Δt_e	4.58
NBQ mode time step (ms)	Δt_q	0.115
Phase-velocity of pseudo-acoustic waves (ms^{-1})	c_s	60
Surface & acoustic wave Courant number	(Co_e, Co_q)	(0.015, 0.0027)
Vertical advection Courant number	Co_w	0.08 (with local “hot spots”)
Equation of state		Compressible and Linear
Kinematic viscosity ($m^2.s^{-1}$)	ν	10^{-5} (horizontally: half of the diffusive part of the upstream advective scheme)
Second viscosity ($m^2.s^{-1}$)	λ	10^2
Asselin Filter Parameter		10^{-3}
Diffusivity ($m^2.s^{-1}$)	K_D	10^{-6}
Open boundary layer		Flow Relaxation Scheme
Forcing M2-tidal period	T_0 (h)	12.4
Coriolis parameters		$(10^{-4}, 0)$

Table 6: Model parameters for Georges Bank experiment (Experiment F).